The Role of Nanometer-Scaled Ligand Patterns in Polyvalent Binding by Large Mannan-Binding Lectin Oligomers

Louise C. Gjelstrup, Jørn D. Kaspersen, Manja A. Behrens, Jan S. Pedersen, Steffen Thiel, Peter Kingshott, Cristiano L. P. Oliveira, Nicole M. Thielens and Thomas Vorup-Jensen

This information is current as of August 4, 2022.

References   This article **cites 72 articles**, 29 of which you can access for free at:
http://www.jimmunol.org/content/188/3/1292.full#ref-list-1

Why *The JI*? Submit online.

- **Rapid Reviews! 30 days*** from submission to initial decision

- **No Triage!** Every submission reviewed by practicing scientists

- **Fast Publication!** 4 weeks from acceptance to publication

*average

Subscription   Information about subscribing to *The Journal of Immunology* is online at:
http://jimmunol.org/subscription

Permissions   Submit copyright permission requests at:
http://www.aai.org/About/Publications/JI/copyright.html

Email Alerts   Receive free email-alerts when new articles cite this article. Sign up at:
http://jimmunol.org/alerts

The Role of Nanometer-Scaled Ligand Patterns in Polyvalent Binding by Large Mannan-Binding Lectin Oligomers

Louise C. Gjelstrup,*[,†,‡,§] Jørn D. Kaspersen,*[,†,‡,§] Manja A. Behrens,[‡,¶] Jan S. Pedersen,[‡,¶] Steffen Thiel,[†] Peter Kingshott,[‡,‖] Cristiano L. P. Oliveira,[‡,¶,#,1] Nicole M. Thielens,**[,1] and Thomas Vorup-Jensen*[,†,‡,§,1]

Mannan-binding lectin (MBL) is an important protein of the innate immune system and protects the body against infection through opsonization and activation of the complement system on surfaces with an appropriate presentation of carbohydrate ligands. The quaternary structure of human MBL is built from oligomerization of structural units into polydisperse complexes typically with three to eight structural units, each containing three lectin domains. Insight into the connection between the structure and ligand-binding properties of these oligomers has been lacking. In this article, we present an analysis of the binding to neoglycoprotein-coated surfaces by size-fractionated human MBL oligomers studied with small-angle x-ray scattering and surface plasmon resonance spectroscopy. The MBL oligomers bound to these surfaces mainly in two modes, with dissociation constants in the micro to nanomolar order. The binding kinetics were markedly influenced by both the density of ligands and the number of ligand-binding domains in the oligomers. These findings demonstrated that the MBL-binding kinetics are critically dependent on structural characteristics on the nanometer scale, both with regard to the dimensions of the oligomer, as well as the ligand presentation on surfaces. Therefore, our work suggested that the surface binding of MBL involves recognition of patterns with dimensions on the order of 10–20 nm. The recent understanding that the surfaces of many microbes are organized with structural features on the nanometer scale suggests that these properties of MBL ligand recognition potentially constitute an important part of the pattern-recognition ability of these polyvalent oligomers. *The Journal of Immunology*, 2012, 188: 1292–1306.

I mmune protection against infection involves molecular mechanisms, which have been evolutionary selected to bind conserved motifs, or "patterns," presented on microbial surfaces (1–3). Mannan-binding lectin (MBL; also known as mannose-binding lectin, mannan- or mannose-binding protein) constitutes a part of the body's protection against infection, as demonstrated by several clinical studies, as well as experimental evidence from animal models focusing on the protective effect in various viral and bacterial infections (4–6). Binding of MBL to microbial patterns activates the complement system, which leads to the deposition of other plasma proteins, notably fragments of complement factor C3, facilitating uptake of microbial agents by leukocytes or direct lysis of membrane-enveloped micro-organisms (1). Consequently, the binding of MBL to appropriate target surfaces is a critical part of immune physiology and clearly a determinant of MBL function; however, a quantitative insight into these processes has been lacking.

The importance of understanding molecular polydispersity in immunology is underscored by the abundance of large proteins, such as Igs, collectins, and ficolins, which contribute to humoral immunity through polyvalent binding to target microbial surfaces. The primary structure of the MBL polypeptide contains an N-terminal segment of 21 residues with three cysteines. This segment is followed by seven collagen-like Gly-Xaa-Yaa repeats, where the residue Xaa is selected from all of the naturally occurring amino acids, and hydroxylated proline or lysine frequently is incorporated as residue Yaa. The collagen-like region is interrupted by a Gly-Gln-Gly sequence, followed by a second collagen-like region with 12 Gly-Xaa-Yaa repeats. This segment is joined at the C terminus to a short, 34-residue neck region and the carbohydrate recognition domain (CRD) of 93 residues, bringing the molecular mass (M) of the monomer to 24,040 Da (7). In the folded molecule, the collagenous regions form a structural unit of three MBL monomers (MBL_3), which are organized into higher-order oligomers through a complex pattern of interchain disulfide bridge formation (8, 9). Several advances in understanding the function of MBL have been made from characterization of the CRD with x-ray crystallography, which explained the selectivity of MBL for certain carbohydrates, such as D-mannose and D-N-

*Biophysical Immunology Laboratory, Aarhus University, DK-8000 Aarhus C, Denmark; †Department of Biomedicine, Aarhus University, DK-8000 Aarhus C, Denmark; ‡Interdisciplinary Nanoscience Center, Aarhus University, DK-8000 Aarhus C, Denmark; §The Lundbeck Foundation Nanomedicine Center for Individualized Management of Tissue Damage and Regeneration, Aarhus University, DK-8000 Aarhus C, Denmark; ¶Department of Chemistry, Aarhus University, DK-8000 Aarhus C, Denmark; ‖Faculty of Engineering and Industrial Sciences, Swinburne University of Technology, Hawthorn, Victoria 3122, Australia; #Department of Physics, University of Sao Paulo, 05315-970 Sao Paulo, Brazil; and **Institut de Biologie Structurale Jean-Pierre Ebel, Centre National de la Recherche Scientifique, Commissariat à l'Energie Atomique, Université Joseph Fourier, 38041 Grenoble Cedex 9, France

[1]C.L.P.O., N.M.T, and T.V.-J. contributed equally to this work.

Address correspondence and reprint requests to Dr. Thomas Vorup-Jensen, Department of Biomedicine, Aarhus University, The Bartholin Building (1240), Wilhelm Meyers Allé 4, DK-8000 Aarhus C, Denmark. E-mail address: vorup-jensen@microbiology.au.dk

Abbreviations used in this article: AFM, atomic force microscopy; CRD, carbohydrate recognition domain; EOM, ensemble optimization method; IFT, indirect Fourier transformation; M, molecular mass; MASP, mannan-binding lectin-associate serine protease; MBL, mannan-binding lectin; MBL_3, three mannan-binding lectin monomers; mcBSA, mannose-conjugated BSA; (neck/CRD)$_3$, trimer of neck/carbohydrate recognition domain; rhMBL, recombinant human mannan-binding lectin; RMSD, root mean square deviation; RU, response unit; SAXS, small-angle x-ray spectroscopy; SPR, surface plasmon resonance; TEA, triethanolamine·HCl.

acetyl glucosamine, but not for others, such as D-galactosamine (10–12). Furthermore, structural characterization of a trimer of neck/CRDs [(neck/CRD)$_3$] showed that the close packing creates an interligand binding site distance of 5 nm (13, 14). Although these findings have shed light on the role of the (neck/CRD)$_3$ in the biology of MBL, in contrast, the role of oligomerization of the MBL$_3$ structural unit is considerably less clear. Structural characterization of native MBL$_3$ oligomers has been carried out with electron microscopy (8), small-angle X-ray scattering (SAXS) (15), and atomic force microscopy (AFM) (15, 16). From these investigations, it is clear that MBL is a highly polydisperse molecule, with the size of the oligomers ranging from three to eight structural units, designated 3×MBL$_3$ and 8×MBL$_3$, respectively (16). However, the structural and functional properties of the various oligomers were difficult to address, because the polydispersity of MBL has proven difficult to overcome by fractionation (8, 17, 18). Consequently, the role of MBL polydispersity in the functions relating to the immune system remains largely unaddressed.

SAXS investigations give structural information on the shape of the molecular envelope in solution (19). The ability to obtain such information from large biomolecular species confers unique possibilities compared with other techniques for obtaining solution structures, such as nuclear magnetic resonance spectroscopy or analytical ultracentrifugation. Consequently, SAXS data can often be used as an important supplement to structural information achieved by other means (20, 21). Bernadó et al. (22) addressed the possibility of obtaining structural information from SAXS on systems with structural heterogeneity in the form of conformational fluctuations in the biomolecules. However, to our knowledge, application of the ensemble optimization method (EOM) in analyses of polydisperse and flexible proteins, such as MBL, has not been attempted previously.

Biosensors based on surface plasmon resonance (SPR) are the leading technology for quantifying the binding kinetics of macromolecular interactions (23). They have been used to measure the binding between MBL and ligands (18, 24, 25), as well the complex formation between MBL and the MBL-associated serine proteases (MASPs) (26). The analysis of the impact of higher-order oligomerization of MBL$_3$ failed to reveal any functional difference between the oligomers, with only an ∼2-fold difference in binding kinetics and equilibrium constants reported for human 3×MBL$_3$ and 4×MBL$_3$ (18). The standard model for analyzing molecular interactions by SPR is based on the assumption of a simple 1:1 first-order reaction (27, 28), often referred to as a pseudo first-order reaction, because the level of complex formation between the molecules in the fluid phase (the analyte) and the surface-exposed ligands is regulated by the concentration of only one of the reactants (i.e., the analyte) (29). As demonstrated by Svitel et al. (30), heterogeneity in ligand binding can be resolved into an ensemble of 1:1 pseudo first-order reactions with a continuous distribution of binding constants. This methodology was used in a number of studies in which the surface-immobilized ligands presented a heterogeneous composition (31–35). As pointed out by Svitel et al. (30), the same methodology also applies for situations in which the analyte is a composition of molecules with heterogeneous ligand-binding properties (e.g., as potentially would be the case for analyzing the avidity of a mixture of MBL$_3$ oligomers). However, such an application of this methodology has not been reported earlier, and the practical usage consequently remains unexplored.

In this study, the oligomeric structure of MBL was investigated with SAXS. By applying the EOM procedure to ion-exchange chromatography-fractionated recombinant human MBL (rhMBL),

we were able to obtain structural information on the oligomerization of rhMBL in these fractions. Using the model by Svitel et al. (30), we derived the binding constants for MBL ligand binding and showed that the number of MBL$_3$ structural units in the complex is critical for the avidity of the ligand binding. Variation in the density of the ligand coating also clearly regulates the binding, pointing to the influence of ligand topology in the promotion of these strong interactions. We report that the oligomerization of MBL$_3$ significantly influences the binding to ligand arrangements with dimensions far larger than 5 nm, which suggests an ultrastructural level of pattern recognition by MBL. These findings point to a role for MBL oligomer polydispersity in providing pattern-recognition molecules with target-recognition abilities suited to a wide range of glycan-presenting surfaces.

Materials and Methods

Fractionation of oligomeric forms of rhMBL

Two preparations of recombinant MBL produced in the mammalian cell line HEK293 (36, 37) were kindly provided by NatImmune A/S (Copenhagen, Denmark). Separation of the MBL oligomers was performed by anion-exchange chromatography with a MonoQ HR 5/5 column (GE Healthcare, Uppsala, Sweden). MBL (1 mg/ml) in a volume of 2 ml buffer A (20 mM Tris-HCl, 50 mM NaCl, 10 mM CaCl$_2$ [pH 8.2]) was applied to the column equilibrated in buffer A. An elution gradient was created in eight steps with 8% (v/v) 20 mM Tris-HCl, 500 mM NaCl, 10 mM CaCl$_2$ [pH 8.2] (buffer B), over an elution volume (V_e) of 30 ml (step 1, referred to in the following as fraction I), followed by 18% (v/v) buffer B over a volume of 199 ml (step 2/fraction II), 20% (v/v) buffer B over 39 ml (step 3), 21.5% (v/v) buffer B over 199 ml (step 4/fraction III), 24% (v/v) buffer B over 38 ml (step 5/fraction IV), 26% (v/v) buffer over 199 ml (step 6/ fraction V), 30% (v/v) buffer B over 39 ml (step 7), and 100% (v/v) buffer B over 19 ml (step 8). Fractions I–V were concentrated in Vivaspin 20 columns (VS2022; Sartorius Stedem, Goettingen, Germany) with an M_r cut-off of 30,000. The MBL oligomers were analyzed by SDS-PAGE and silver staining, as described elsewhere (38).

Production of recombinant (neck/CRD)$_3$ in insect cells

The cDNA encoding the trimerizing neck region and the CRD was PCR amplified from the pC1-MBL construct (36) with cDNA encoding the complete MBL sequence with forward primer 5′-CGG GAT CCG GAT GGT GAT AGT AGC CTG G-3′ and reverse primer 5′-GGA ATT CTC AGA TAG GGA ACT CAC AGA CGG-3′ (Eurogentec SA, Seraing, Belgium), which added a BamHI and an EcoRI restriction site (indicated by underscored characters). The thermal program consisted of one incubation at 95°C for 10 min, followed 29 cycles with 95°C for 1 min, 57°C for 1 min, and 72°C for 1 min and terminated by incubation at 72°C for 2 min using Vent polymerase (New England Biolabs, Ipswich, MA). Cloning of the PCR products into the pNT-Bac vector was carried out as described (39). The recombinant donor plasmid (pNT-Bac–recombinant neck/CRD) was transformed into DH10Bac *Escherichia coli* strain (Invitrogen, Carlsbad, CA). Selection of a bacmid, with the pNT-Bac vector correctly inserted, was performed using media containing kanamycin, tetracycline, and gentamicin. Following transfection of Sf21 cells, the viral stock was collected and used for infection of High Five cells, carried out as described (40). The culture supernatant from baculovirus-infected High Five cells was dialyzed against 40 volumes 145 mM NaCl, 5 mM CaCl$_2$, 50 mM triethanolamine·HCl (TEA) (pH 7.4). A 10-ml D-N-acetyl glucosamine-derivatized agarose matrix (41) was equilibrated in 50 mM TEA, 145 mM NaCl, 5 mM CaCl$_2$ (pH 7.4), and the supernatant was passed through the beads. Following washing of the column, bound recombinant (neck/CRD)$_3$ were eluted with 0.3 M D-N-acetyl-glucosamine in the same buffer. Protein-containing fractions, identified by UV light absorption at λ = 280 nm, were pooled and dialyzed against 145 mM NaCl, 5 mM CaCl$_2$, 50 mM TEA (pH 7.4) to remove the eluent.

Analysis of the solution structure of recombinant (neck/CRD)$_3$ and fractionated rhMBL by SAXS

SAXS measurements on recombinant MBL (neck/CRD)$_3$ and fractions of intact rhMBL were performed with a flux- and background-optimized prototype of the NanoSTAR SAXS camera (Bruker AXS, Madison, WI) (42). The equipment was set up in a high-resolution configuration, which enables the measuring q range of 0.004 Å^{-1} < q < 0.211 Å^{-1}, with q =

$(4\pi/\lambda)\sin\theta$, where 2θ is the scattering angle and λ is the radiation wavelength of 0.15 nm. Samples were loaded into a reusable quartz capillary mounted in a home-made stainless steel holder and kept at 20˚C. The human (neck/CRD)$_3$ sample and the samples of fractionated rhMBL were dialyzed against 140 mM NaCl, 10 mM Tris-HCl (pH 7.4), and this buffer was used as a baseline reference in the SAXS analyses. Samples of protein were applied at concentrations (determined from the light absorption at 280 nm) of 7.5 and 2.5 mg/ml to check for concentration-dependent protein–protein interactions. All samples were analyzed in capillaries ~2 mm in diameter. Data on protein-containing samples were collected for 4–9 h and for 2 h for the background sample. The scattering intensity of the buffer was subtracted from the intensity of the protein-containing samples. The analysis of the data, including the use of the EOM procedure, is described below, together with the experimental findings, in the *Results* section.

SPR spectroscopy of the ligand-binding kinetics of MBL$_3$ oligomers and the (neck/CRD)$_3$ fragment

The binding of the MBL$_3$ oligomers or recombinant (neck/CRD)$_3$ to ligand-coupled surfaces was assessed with SPR spectroscopy using the BIAcore 3000 instrument (GE Healthcare). BSA conjugated with mannose (cat. no. NP01-01, lot. no. 180905M0225-1) was bought from Dextra (Reading, U.K.). On average, each BSA molecule carried 28–32 mol mannose/mole BSA. Mannose-conjugated (mc)BSA was diluted to 30 μg/ml in 10 mM sodium acetate (pH 4) and immobilized on the surface of a CM5 sensor chip (Biacore AB) through amine coupling (Amine coupling kit, cat. no. BR-1000-50; BIAcore). The carboxymethylated dextran layer in the four flow cells formed on the chip surfaces was coupled with 600, 1600, and 4000 resonance units (RU) of mcBSA, together with a reference surface containing 2300 RU of unconjugated BSA. Experiments were performed with a running buffer containing 145 mM NaCl, 2 mM CaCl$_2$, 50 mM Tris-HCl (pH 7.4) with 0.005% (v/v) surfactant P20 (Biacore AB) at a flow rate of 20 μl/min and a data-collection frequency of 1 Hz. Dilutions of MBL$_3$ oligomers or recombinant (neck/CRD)$_3$ oligomers were injected over a period (or contact time) of 180 s, followed by collection of data on the release of the oligomers for 180 s. Because the binding of MBL is strictly calcium dependent, the surfaces were regenerated after each run by injection of 145 mM NaCl, 5 mM EDTA, 50 mM Tris-HCl (pH 7.4) with 0.005% (v/v) surfactant P20.

A self-assembled monolayer of 11-mercaptoundecanoic acid (Sigma-Aldrich) on gold was used for probing the interaction between MBL$_3$ oligomers and surface ligands. Unmodified gold-sensor chips (BR-1005-42; Sensor Chip AU) were bought from GE Healthcare. Before functionalizing the surfaces, the gold crystals were cleaned using the following procedure: the crystals were treated with UV-ozone for 30 min and then immersed in 20 ml ultrapure water (Millipore, Billerica, MA) in a small beaker, which had been cleaned in 2% (w/v) SDS and ultrapure water. A mixture of H$_2$O, NH$_4$OH, and H$_2$O$_2$ was made at a ratio of 5:1:1 ratio and heated to 70˚C. The gold crystals were incubated in it at 70–80˚C for 5 min, rinsed with ultrapure water, and finally dried in N$_2$ gas, followed by UV-ozone treatment for 20 min.

The Teflon bottles used for functionalizing the surfaces were cleaned by sonication for 30 min with 2% (w/v) SDS dissolved in ultrapure water, followed by rinsing in ultrapure water and drying in N$_2$ gas. The crystals were immersed in the bottles containing a solution of 1 mM 11-mercaptoundecanoic acid in pure ethanol (HPLC grade) and stored at room temperature for 40 h. After removing the crystals from the solution, they were sonicated in pure ethanol for a few minutes to remove unbound molecules and dried in N$_2$ gas.

The analysis of the SPR data, by use of both the 1:1 pseudo first-order reaction, as well as the procedure described by Svitel et al. (30), are described below, together with the experimental findings, in the *Results*.

Results

Fractionation of rhMBL oligomers and synthesis of a (neck/CRD)$_3$ MBL fragment

To enable the structural and functional analyses described in the sections below, both intact MBL$_3$ oligomers and a fragment containing a trimer of the CRD were prepared.

Fractionation of the rhMBL oligomers was carried out by anion-exchange chromatography with a slow, step-wise elution (Fig. 1A) in large volumes of elution buffer (i.e., 100–200 column volumes for each step). Analysis of the fractions under denaturing conditions by SDS-PAGE and silver staining of the gel-embedded

proteins revealed a considerable size heterogeneity of the protein species; however, large MBL species (i.e., $M > 250$ kDa) were enriched relative to the abundance of smaller MBL species in fractions IV and V compared with fractions I–III (Fig. 1B).

Recombinant (neck/CRD)$_3$ was produced in insect cells. The integrity of the primary structure and purity of the (neck/CRD)$_3$ was analyzed by SDS-PAGE (Fig. 1C), which showed that the recombinant material matched the expected M at 16,399 Da and that the material was largely a pure preparation. The apparent M of the protein was slightly increased in samples in the reduced state compared with the nonreduced state (Fig. 1C), as reported earlier for a construct similar to ours (43). The MBL CRD contains two intramolecular disulphide bridges. Even in the presence of denaturant, such as SDS, these bridges would be expected to keep the structure of the domain more compact, permitting faster migration under SDS-PAGE compared with the lack of structure obtained by reduction and presence of denaturant. Consequently, the faster migration of the nonreduced sample indicated that the domain had correctly formed intramolecular disulphide bridges, as was also suggested from an analysis made on engineered disulphide bridges introduced in integrin I domains (44). The identity and integrity of the construct was further confirmed by MALDI mass spectroscopy, where the M of [M+H$^+$] species was determined to be 16,391 $\pm$ 12 Da (data not shown). N-terminal sequencing yielded an unambiguous DPDGSSL sequence (data not shown) (i.e., an aspartate residue added from in-frame cloning of the MBL sequence with a mellittin signal peptide, followed by residues 101–106 of the polypeptide chain of MBL). Properties of the quaternary structure were analyzed under native conditions by gel-permeation chromatography; the protein eluted at a volume close to the elution volume for OVA (Fig. 1D), a globular protein with an M of 42,700 Da and a hydrodynamic radius of 3.0 nm (45).

A closer evaluation of the structure was achieved by analysis of the SAXS data of the recombinant (neck/CRD)$_3$. The experimental curve was compared with the theoretical intensity calculated by the CRYSOL (version 2.6) program package (46) from the atomic-resolution structure of the human (neck/CRD)$_3$ determined by x-ray crystallography (Brookhaven Protein Data Bank entry 1HUP) (13) (Fig. 1E). A near-complete agreement was found between the experimental and theoretical intensity.

Spectral properties of fractionated rhMBL subjected to SAXS

SAXS data from fractions I–V of rhMBL were recorded; the experimental data in Fig. 2A are represented by open symbols. A simple way of obtaining structural information about the compactness of the structure from the SAXS spectrum is by use of the so-called "Kratky plot," $q^2 \times I(q)$ versus q (Fig. 2B), where q is the modulus ("length") of the scattering vector. In this representation, highly folded, globular protein species show a bell-shaped curve, with a maximum in the low q region. Unfolded and flexible species show a plateau or a steady increment in the product $q^2 \times I(q)$ at high q, depending on the level of flexibility (47). The data in Fig. 2B show a well-defined maximum around $q \sim 0.06$ Å^{-1}, followed by a plateau at higher q values. Other studies showed that such data are typical of flexible multidomain proteins (47). Importantly, the curves for the five fractions could be superimposed, indicating that structural content and flexibility level of the molecular species in these fractions were similar.

A closer characterization of the experimental data was made by indirect Fourier transformation (IFT), using the method developed by Glatter (48) in a modified implementation (49, 50). From the IFT transformations, indicated with solid black lines in Fig. 2A, the pair distance distribution function, $p(r)$ (Fig. 2C), the radius of
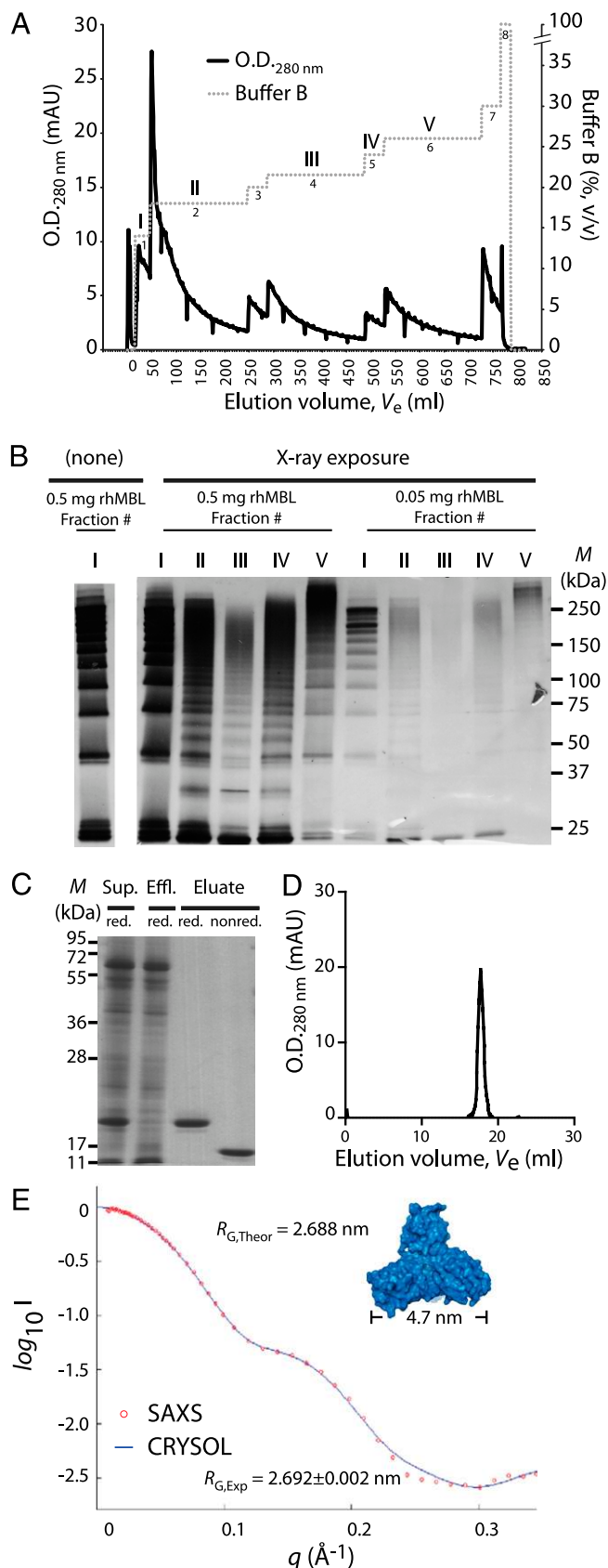
FIGURE 1. Fractionation of intact and fragments of rhMBL. *A*, Ion-exchange chromatography fractionation of MBL₃ oligomers. Recombinant MBL was loaded onto the anion-exchange column equilibrated in a low-salt buffer. The bound protein was eluted through increment of the salt concentration in eight steps. These are represented by Arabic numerals and a dotted line showing the percentage of the high-salt buffer B. The elution of protein was monitored by absorption at OD$_{280\ nm}$ (black line). The collected fractions are indicated with Roman numerals I–V. *B*, SDS-PAGE of fractionated rhMBL before and after x-ray exposure during collection of the SAXS data. The exposed fractions were applied to the gel at 0.5 and 0.05 mg for fractions I–V as indicated, followed by silver staining of the gel. *C–E*, Purification and structural characterization of the (neck/CRD)₃. *C*, The cell supernatant, effluent, and eluate from synthesis of the (neck/CRD)₃ were analyzed by SDS-PAGE in the reduced (red.) or nonreduced (non-red.) state. *D*, Gel permeation chromatography analysis of purified (neck/CRD)₃. *E*, Analysis of the (neck/CRD)₃ structure by SAXS. The structure of human (neck/CRD)₃ (13), determined by x-ray crystallography (Brookhaven Protein Data Bank accession code 1HUP), was applied to the CRYSOL algorithm (46) for calculation of the expected SAXS curve. Experimental and predicted spectrum (indicated with open red circles and blue line, respectively) are shown, with the scattering intensity (*I*) plotted as a function of the inverse modulus of the scattering vector *q*. The theoretically calculated radius of gyration ($R_{G,Theor}$) is indicated, together with the experimental value ($R_{G,Exp}$). Scale bar shows the distance between Asp[206] in two CRD domains in the (neck/CRD)₃.

gyration (R_G), and an extrapolation to the forward scattering, $I(0)$, were obtained. Because the data are normalized to absolute scale, the molecular masses of the molecules in solution were calculated from the forward scattering:

$$M_W^{protein} = \frac{I(0)}{\rho_{MBL} \cdot (\Delta\rho_m)^2} N_A, \qquad (1)$$

where $M_W^{protein}$ is the absolute weight-average molecular mass of the protein, ρ_{MBL} is the mass protein concentration, $\Delta\rho_m$ is the scattering length density difference per unit mass for which a standard value of 2.0×10^{10} cm/g was used, and N_A is Avogadro's number. R_G was determined from the calculation of the second moment of the pair distance distribution function,

$$R_G{}^2 = \frac{\int p(r)r^2 dr}{2\int p(r)dr}. \qquad (2)$$

The obtained parameters are listed in Table I. A clear increase was observed in M, the maximum dimension (D_{Max}), and average R_G with fraction number. Consequently, the ion-exchange chromatography fractionation enriched the larger oligomers in fractions III and IV compared with fractions I and II, as was also found in the analysis of the oligomers under denaturing conditions (Fig. 1*B*). Comparison of the MBL species before and after SAXS showed no indication of molecular degradation as a consequence of the exposure to radiation (Fig. 1*B*).

Modeling shape, flexibility, and polydispersity of fractionated rhMBL oligomers from EOM-based analysis

In the study by Dong et al. (15) a pseudo-atomic model for the structure of the 3×MBL₃ oligomer was made from SAXS measurements on unfractionated rhMBL. The structure was assumed to be rigid and have a 3-fold rotational symmetry axis. However, the rigidity introduced a significant limitation in the modeling procedure, because the flexibility in the orientation of the arms could not be properly introduced in the structural searches. Furthermore, a broadening of the envelope at the site of the (neck/CRD)₃ caused some interpretational challenges in comparison with the crystallographic data describing the structure of this fragment (13, 14). Available biochemical evidence suggested that the broadening could be explained as a consequence of the flexible attachment of the (neck/CRD)₃ to the collagenous stalks, but a direct test of this hypothesis was not performed (15). These questions concerning the solution structure of MBL were
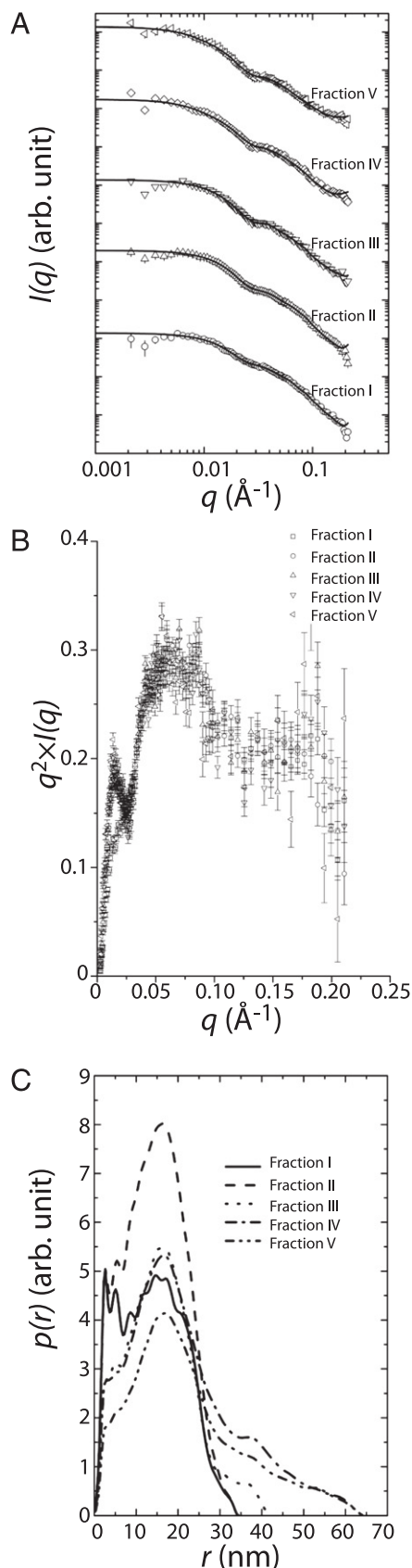
FIGURE 2. SAXS measurements on fractionated rhMBL. *A*, Fits to the data by the IFT procedure (48–50). Open circles indicate the experimental scattering intensity in arbitrary units as a function of q. Solid lines show fitting of these data obtained with the IFT procedure. *B*, Kratky plot with the scattering profile intensity, $I(q)$, multiplied by the square of the modulus of the scattering wave vector, q, plotted versus q. Plots were made for

addressed by novel computational approaches to SAXS data, as described below.

In the present work, the EOM procedure (22) was applied to model the experimental SAXS data for MBL fractions. In the original implementation, the EOM procedure does not permit the use of multiple models in the optimization procedure, because only one model with a fixed number of residues is permitted. However, because the genetic algorithm optimization (22) combines individually the scattering curves for each conformation of the model, an initial pool comprising more than one model can be constructed and analyzed. On the condition of sufficient differences in scattering properties among the pooled models, the optimization procedure selects ensembles of each model with conformations that give the best fit of the spectra. By analyzing the selected species, it is possible to obtain the fractional inclusion (*f*) of each model, as well as D_{Max} and R_G for the selected species of each model.

Models of $3{\times}MBL_3$ and $6{\times}MBL_3$ were built from the structure suggested earlier by Dong et al. (15) for $3{\times}MBL_3$. Consistent with experimental data suggesting collagen to form a stable structure with small-amplitude internal motions and a rigid peptide backbone (51), the collagenous stalks were modeled as rigid with a flexible attachment at the C termini to the $(neck/CRD)_3$, with the structure determined by x-ray crystallography. At the N termini, the rigid collagenous stalks were joined with flexible linkers. Because the original EOM procedure (22) works on the assumption that the protein species is composed of a single chain, it does not permit the construction of a multi-chain model. However, by proper editing of the input model file, it was possible to build multi-chain models composed of three or six MBL_3 structural units in such a way that the EOM procedure treated the pool as being composed of molecules containing a single chain. For both the model with three and six MBL_3 structural units, the structural units were connected at the N termini.

In an initial analysis, we considered the SAXS spectrum produced by such two types of MBL oligomers. From the EOM procedure, the theoretical scattering curve from the selected ensemble of these two components is obtained. At this step, the scattering intensity is described by

$$I(q) = S_{C_1} \cdot P_{model}(q) + b, \qquad (3)$$

where S_{C1} is the scale factor, $P_{model}(q)$ is the average form factor, and b is the corrected background scattering. With the subtraction of the scattering from the buffer, the fitted values of b were, in general, small [i.e., $S_{C1} \cdot P_{model}(q) \gg b$]. In this initial approach, no interaction between the molecules was assumed; therefore, structure factor effects were neglected (52). The optimization program was allowed to vary the spatial arrangement of the stalks and $(neck/CRD)_3$. As a first step, using the program "Random Chain" (22), two populations were made, consisting of 7500 conformations for each of the $3{\times}MBL_3$ and $6{\times}MBL_3$ oligomers, which generated a size list and an intensity file with 7,500 intensity curves (i.e., one for each MBL oligomer conformation). The populations of $3{\times}MBL_3$ and $6{\times}MBL_3$ oligomers were joined in a single size list and intensity file, containing the maximal permitted number

the scattering profile obtained for fractions I–V. *C*, Distribution, in intramolecular distances, of the MBL fractions. The intramolecular distances between atoms in molecular envelope, *r*, were derived from the IFT procedure. The distance distribution, $p(r)$, was plotted as a function of the distance *r* for fractions I–V.

Table I. Structural parameters of the MBL$_3$ oligomers in fractions I–V determined by SAXS

Sample	R_G (nm)^a	D_{Max} (nm)^a	M (kDa)^b	ρ_{MBL} (mg/ml)
Fraction I	11.3 ± 0.10	35	288 ± 14	6.5
Fraction II	11.5 ± 0.10	35	464 ± 25	5.8
Fraction III	12.8 ± 0.21	43	553 ± 50	3.4
Fraction IV	18.0 ± 0.33	65	725 ± 68	3.3
Fraction V	18.5 ± 0.45	65	979 ± 158	1.9

^{a}Determined from $p(r)$ and Eq. 2.
^{b}Determined from Eq. 1.
ρ_{MBL}, mass concentration of MBL$_3$.

(15,000) of conformations and intensity curves. These data were submitted to the program "Genetic Algorithm Judging Optimization of Ensembles" (22), which selects a subset of the conformations that gives the best fit of the scattering intensity.

The agreement between the calculated model [i.e., with the average form factor $P_{model}(q)$ indicated with a broken line] and the experimental data is shown in Fig. 3A. The distributions in R_G and D_{Max} for the selected ensemble of conformations of 3×MBL$_3$ and 6×MBL$_3$ oligomers are shown in Fig. 3B. The distribution in R_G and D_{Max} for 3×MBL$_3$ showed major peaks at 11 and 32 nm, respectively, in good agreement with the values published earlier (15). However, the distribution of R_G was not symmetric, because distinct, albeit smaller, peaks were also found at 8 and 13 nm (Fig. 3B). The conformations of the selected 6×MBL$_3$ ensemble presented a distribution of R_G and D_{Max} with peaks at 14 and 42 nm, respectively. The structural properties of the conformers of 3×MBL$_3$ and 6×MBL$_3$ are indicated in Fig. 3C and Fig. 3D, respectively. For both oligomers, a considerable variation in the orientation and conformation of the arms was found. Some of the 3×MBL$_3$ con-

formers extended in a near-planar conformation, whereas others showed a more diverse orientation of the arms. Furthermore, with regard to the orientation of the (neck/CRD)$_3$ relative to the stalks, this appeared as flexible when comparing the shown ensemble of 3×MBL$_3$ and 6×MBL$_3$ conformations. Interestingly, the use of the (neck/CRD)$_3$ structural coordinates derived from x-ray crystallography and analyzed further by SAXS with soluble (neck/CRD)$_3$ (Fig. 1E) produced a good fitting of the experimental data in the interval of 0.01 Å^{-1} < q < 0.1 Å^{-1} for all fractions (Fig. 3A). By contrast, attempts to account for the broadening of the molecular envelope by tilting the orientation of neck helices in the (neck/CRD)$_3$, as described by Dong et al. (15), led to a considerably worse fit in the entire measured interval (data not shown). Thus, the ensemble of conformations with a flexible orientation of the (neck/CRD)$_3$ appeared to account for the experimental results. Therefore, analysis of the SAXS spectra by the EOM agreed with the Kratky plot analysis, suggesting that intrinsic flexibility is indeed part of the solution structure of intact MBL oligomers, and the broadening found previously was an artifact of modeling the structure as rigid. From the genetic algorithm optimization, it was found that the fractionation of rhMBL (Fig. 1A, 1B) led to an increase in the fraction of 6×MBL$_3$ with increasing elution volume. As shown in Table II, the frequencies of 3×MBL$_3$ and 6×MBL$_3$ oligomers (designated $f_{3×MBL3}$ and $f_{6×MBL3}$) were 0.9 and 0.1, respectively, in fraction I. In fraction III and at larger elution volumes, this situation was reversed, with a complete dominance of 6×MBL$_3$ oligomers (i.e., $f_{6×MBL3}$ ~1).

Supramolecular assemblies of MBL oligomers

Although the EOM approach provided a reasonable fit for the experimental data, the best fit was accomplished for fraction I, for which nearly the entire curve is well fitted. For fractions III–V, some
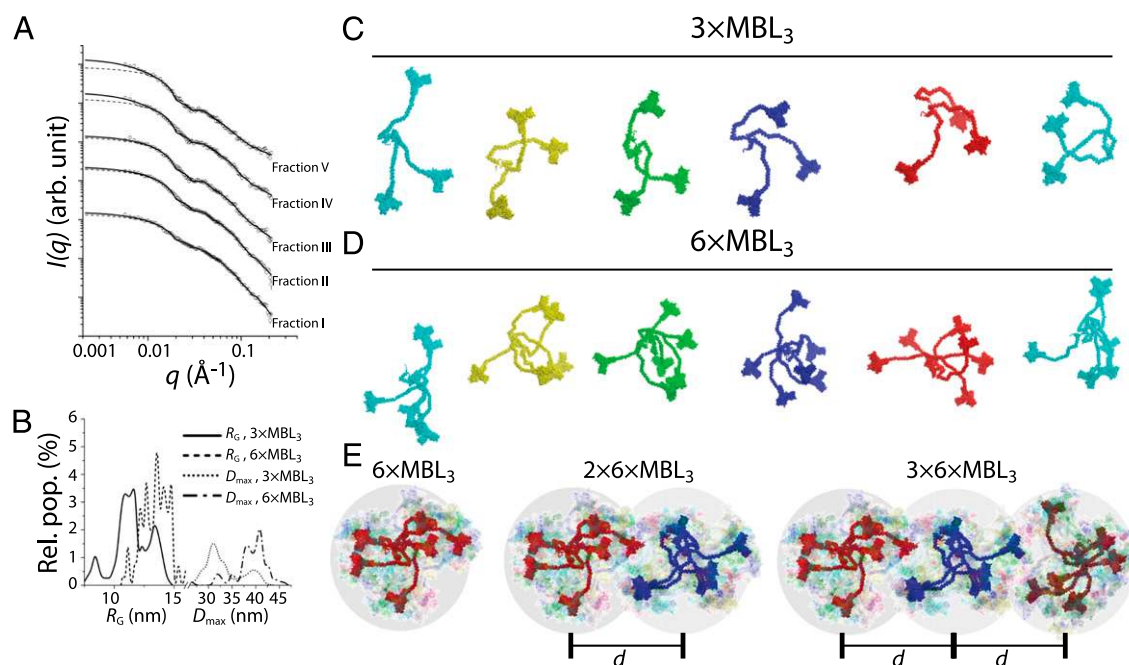

FIGURE 3. EOM analysis of the oligomeric distribution of MBL in fractions I–V. The EOM procedure of Bernadó et al. (22) was modified, as detailed in the text. A, Experimental SAXS data for fractions I–V (○) were fitted by using ensembles of 3×MBL$_3$ and 6×MBL$_3$ oligomers. The predicted scattering profile for ensembles is indicated by dashed lines. The fit to the data were further improved by including assemblies of the 3×MBL$_3$ and 6×MBL$_3$ oligomers. The expected scattering profile of such assemblies, together with the ensembles of 3×MBL$_3$ and 6×MBL$_3$ oligomers, is indicated by the black line. B, The distribution in R_G and D_{Max} for the ensemble of 3×MBL$_3$ and 6×MBL$_3$ oligomers. Examples of the quaternary structure of the 3×MBL$_3$ (C) and 6×MBL$_3$ (D) oligomers in the ensemble determined by the EOM procedure. E, Representation of the structural properties of the supramolecular assemblies of the 6×MBL$_3$ oligomers. The envelope of 6×MBL$_3$ oligomers is indicated, together with two examples (red and blue) of quaternary structures of these oligomers. The supramolecular assemblies were made by joining two or three 6×MBL$_3$ oligomers separating the center of the oligomers by a distance d.

Table II. Distribution of 3×MBL₃ and 6×MBL₃like oligomers in fractions I–V

| | EOM Analysis[a] | | | | | | $S_{tot}(q) = f_{mon} + f_{dim} \cdot S_{dim}(q) + f_{trim} \cdot S_{trim}(q)$[b] | | | |
| | 3×MBL₃ | | | 6×MBL₃ | | | Supramolecular Interactions | | | |
Sample	R_G (nm)[c]	D_{Max} (nm)[d]	$f_{3\times MBL3}$[e]	R_G (nm)[c]	D_{Max} (nm)[d]	$f_{6\times MBL3}$[f]	f_{mon}[g]	f_{dim}[g]	f_{trim}[g]	d (nm)[h]
Fraction I	11.5 ± 1.5	32.3 ± 4.7	0.9	13.4 ± 1.1	38.9 ± 3.6	0.1	0.93	0.07	0.00	24.0 ± 1.4
Fraction II	10.5 ± 1.4	29.4 ± 3.9	0.24	13.1 ± 1.1	38.4 ± 3.4	0.76	0.94	0.06	0.00	23.0 ± 1.7
Fraction III	–	–	0.0	13.0 ± 1.1	38.3 ± 3.5	1.0	0.94	0.06	0.00	23.6 ± 2.4
Fraction IV	–	–	0.0	13.2 ± 1.0	38.6 ± 3.5	1.0	0.90	0.00	0.10	22.5 ± 0.8
Fraction V	–	–	0.0	12.6 ± 0.9	37.0 ± 2.9	1.0	0.86	0.00	0.14	22.1 ± 0.8

[a]Results from EOM analysis determining the ensemble of 3×MBL₃- and 6×MBL₃-like oligomers required to fit the scattering profiles of fractions I–V.
[b]Modification of the structure factor, S_{tot}, required to fit the scattering profile for $q > 0.1$ Å^{-1}.
[c]Mean R_G (± SD) for 3×MBL₃- or 6×MBL₃-like oligomers included in the selected ensemble.
[d]Mean D_{Max} (± SD) for 3×MBL₃- or 6×MBL₃-like oligomers included in the ensemble.
[e]Fraction of 3×MBL₃-like oligomers in the selected ensemble of oligomers.
[f]Fraction of 6×MBL₃-like oligomers in the selected ensemble of oligomers.
[g]Fractional distribution of supramolecular assemblies modifying the structure factor, according to Eq. 4.
[h]Distance separating the oligomeric constituents of the supramolecular assemblies.

deviations between the model curve and the data were observed in the low q region ($q < 0.01$ Å^{-1}). This disagreement is related to the formation of larger complexes. As indicated by the IFT analysis (Fig. 2A), fractions II–V contained large structures, as suggested by the large values of D_{Max}, R_G, and M (Table I). The maximum size of 3×MBL₃ and 6×MBL₃ conformers was reached for structures in which the arms are fully extended. However, these conformers would not be able to account for the values of D_{Max}, R_G, and M determined for the molecules, in particular in fractions IV and V. A further increase in the number of structural units in the oligomers included in the ensemble (e.g., by inclusion of 7×MBL₃ or 8×MBL₃ oligomers) would not improve the fitting either, because the maximum values of D_{Max} and R_G for these structures are similar to 6×MBL₃ as a result of the centrosymmetric organization of the oligomers. We analyzed the data by testing the hypothesis that intermolecular interactions created supramolecular assemblies. As an example of such assemblies, a dimer of 6×MBL₃ oligomers ("2 × 6×MBL₃") and a trimer ("3 × 6×MBL₃") are shown in Fig. 3E. These were modeled with a separation of the assembled MBL oligomers by the distance d. The frequency and ultrastructural properties of such supramolecular assemblies were analyzed by introducing the structure factor, $S_{tot}(q)$, to contain a linear combination of structure factors for monomers, dimers, and trimers of the MBL oligomers:

$$S_{tot}(q) = f_{mon} + f_{dim} \cdot S_{dim}(q) + f_{trim} \cdot S_{trim}(q), \quad (4)$$

where $\sum_k f_k = 1$,

$$S_{dim}(q) = 2 + 2\frac{\sin(qd)}{qd}, \quad (5)$$

and

$$S_{trim}(q) = 3 + 4\frac{\sin(qd)}{qd} + 2\frac{\sin(2qd)}{2qd}. \quad (6)$$

With these modifications, the SAXS data were modeled by modifying Eq. 3 to

$$I(q) = S_{C_1} \cdot P_{model}(q) \cdot S_{tot}(q) + b. \quad (7)$$

To reduce the number of variable introduced in the analysis, the average form factor, $P_{model}(q)$, was taken as that of the ensembles of conformations of 3×MBL₃ and 6×MBL₃, as obtained from the EOM procedure. During the fitting of Eq. 7 to the experimental data, the overall scale factor, S_{C_1}, the fractional abundance, f_j, the distance between monomers, d, and the background parameter, b, were optimized.

The introduction of supramolecular assemblies considerably improved the modeling of the experimental data, not only for the low angle part, $q < 0.01$ Å^{-1} compared with using the pure form factors derived from the EOM (Fig. 3A). For all fractions, the supramolecular assemblies had frequencies <0.14, suggesting that molecular species were dominated by monomers of 3×MBL₃ and 6×MBL₃ oligomers (Table II). In fraction I, dimeric species had a frequency of 0.07, probably mainly representing assemblies of $2 \times 3\times MBL_3$, because 3×MBL₃ oligomers dominated this fraction ($f_{3\times MBL3} = 0.9$). In fraction III, which consisted almost entirely of 6×MBL₃ ($f_{6\times MBL3} = 1.0$), dimeric assemblies (i.e., $2 \times 6\times MBL_3$) (Fig. 3E) were present with a frequency of 0.06. In fractions IV and V, which also were nearly pure 6×MBL₃, even larger assemblies of $3 \times 6\times MBL_3$ (Fig. 3E) had a frequency of 0.10–0.14. Interestingly, for all assemblies, a value of d in a narrow interval of 22–24 nm was found, suggesting a conserved interoligomeric distance for both dimers and trimers of the MBL oligomers, as well as for assemblies of either 3×MBL₃ or 6×MBL₃ oligomers. Although other types of supramolecular arrangements cannot be excluded, this simple procedure enabled a very good fit of the experimental scattering data.

Establishing an SPR spectroscopy-based assay for quantifying the binding between MBL oligomers and ligands

SPR spectroscopy has been used for studies of the interaction between MBL and ligands (18, 24). Based on the observation made earlier that mcBSA supports stronger MBL binding than does *N*-acetyl glucosamine-conjugated BSA, we prepared SPR chip surfaces with mcBSA. The ligand density was measured by the response level (S_I) following covalent immobilization of ligand to the carboxymethylated dextran on the CM5 chip surface. The surfaces were made with three densities of coupled ligand: low density ($S_I = 600$ RU), intermediate density ($S_I = 1600$ RU), or high density ($S_I = 4000$ RU), where 1000 RU equals 1 ng of surface-bound protein/mm^2. To monitor nonspecific binding, a reference surface was prepared by coupling unconjugated BSA onto a flow cell surface, which also permitted an optimization of the running buffer to obtain minimal nonspecific binding. Running buffers with 20 mM HEPES, 20 mM Tris-HCl, or 50 mM Tris-HCl (with the same salt concentrations and pH) were compared. The nonspecific binding observed with a running buffer of 20 mM Tris-HCl or 20 mM HEPES disappeared when the 50 mM Tris-HCl buffer was used (data not shown). However, bulk changes in

the refractive index were still observed at the time of starting the injection of MBL (data not shown). As pointed out by Karlsson and Fält (53), bulk changes in SPR signal (S) are dependent on the type of protein injected and differences in salt concentration between the running buffer and the injected buffer. Using the signal from the reference flow cell, such effects were removed from the analysis of the binding kinetics by simple subtraction.

A particular challenge exists with regard to relating the mass-per-volume concentration of MBL in fractions I–V to a molar concentration, bearing in mind the polydispersity of these samples with regard to MBL oligomerization. To provide a simple way of comparing the binding of the MBL oligomers in these fractions on a molar scale, we based the analyses below on the molar concentration of MBL_3 structural units (c_{MBL3}).

$$\sum_n n \cdot c_{n \times MBL_3} = c_{MBL_3}, \quad (8)$$

where $c_{n \times MBL_3}$ is the concentration of oligomers with n structural units. For each fraction I–V, c_{MBL3} was easily determined from the mass concentration (ρ_{MBL}) (Table I), with $c_{MBL3} = \rho_{MBL}/M_{MBL3}$, where M_{MBL3} is the molar mass of MBL_3 of 72,120 Da.

Binding kinetics of MBL_3 oligomers to mcBSA-coated surfaces analyzed as a 1:1 pseudo first-order reaction

The size-sorted MBL_3 oligomers were injected over a surface coupled with 1600 RU of mcBSA (Fig. 4). The sensorgrams followed the expected shape, with an increase in the SPR signal (S) during the contact time, indicating increasing deposition of the oligomers, followed by a declining signal after the end of injection from the gradual loss of bound molecules from the surface. For each of the fractions I–V, five or six concentrations were applied, with a clear increase in the signal with increasing concentration (Fig. 4). None of the injections led to a steady-state equilibrium during the injection phase.

The classic approach for evaluating the SPR sensorgrams expressing the binding of proteins to surface-immobilized ligands is based on the assumption that complexes form with a 1:1 stoichiometry in a simple pseudo first-order reaction (27, 28). The binding

kinetics of this reaction relate the signal at time point t, the rate of association (k_a), the rate of dissociation (k_d), and the constant protein concentration (c_{MBL3}) in the flow stream during the injection phase as:

$$S(k_a, k_d, c_{MBL_3}, t) = \frac{c_{MBL_3} \cdot S_{Max}}{c_{MBL_3} + \frac{k_d}{k_a}} (1 - e^{-(k_a \cdot c_{MBL_3} + k_d) \cdot (t - t_0)}), \quad (9)$$

where S_{Max} is the SPR signal at binding saturation, and t_0 is the time point at the start of injection. With the dissociation constant, K_D, defined by the kinetic constants:

$$K_D = \frac{k_d}{k_a}, \quad (10)$$

Eq. 9 can be written as:

$$S(k_d, K_D, c_{MBL_3}, t) = \frac{c_{MBL_3} \cdot S_{Max}}{c_{MBL_3} + K_D} \cdot (1 - e^{-\frac{k_d}{K_D} (c_{MBL_3} + K_D) \cdot (t - t_0)}). \quad (11)$$

Following the injection phase, ending at time point t_c, the refractive index follows an exponential decay defined by

$$S(k_d, K_D, c_{MBL_3}, t) = \left(\frac{c_{MBL_3} \cdot S_{Max}}{c_{MBL_3} + K_D} \cdot (1 - e^{-\frac{k_d}{K_D} (c_{MBL_3} + K_D) \cdot (t_c - t_0)}) \right) \cdot \left(e^{-k_d \cdot (t - t_c)} \right). \quad (12)$$

This model was fitted to the sensorgrams shown in Fig. 4 using the BIAeval algorithm (GE Healthcare). To avoid any influence from the noise generated at the start and end of the injection phase, data included for the modeling started at approximately t_0 5 s to $t_c - 5$ s for the injection phase and from $t_c + 5$ s to $t \sim 450$ s for the dissociation phase. Because bulk changes in the refractive index during injection of MBL_3 oligomers were corrected by subtraction of the signal from the reference flow cell, the algorithm was forced to fit sensorgrams without a discontinuous change in signal at injection stop (i.e., at t_c). The modeling was carried out as
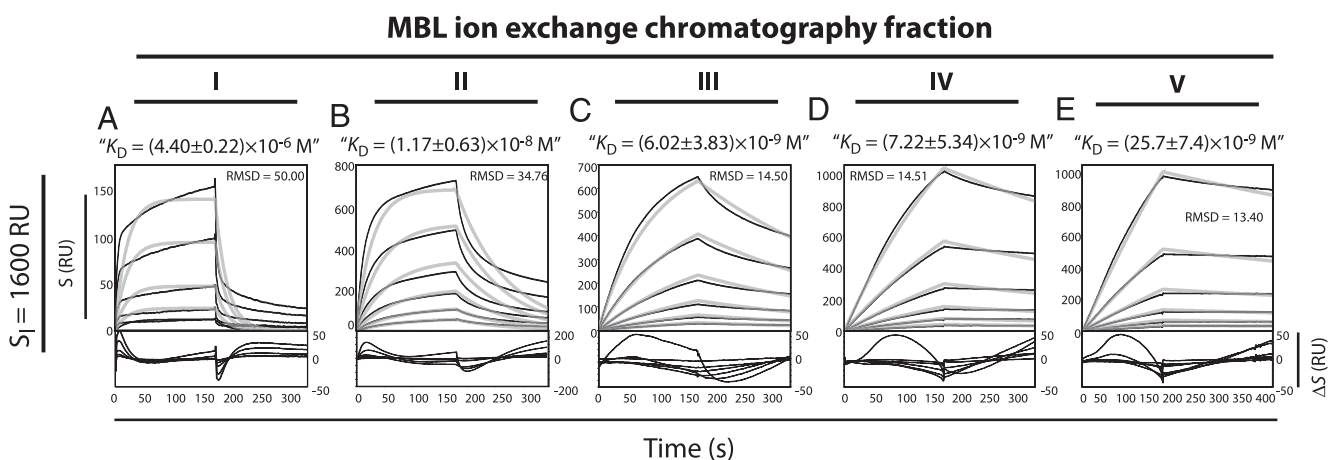
MBL ion exchange chromatography fraction

FIGURE 4. Analysis of the binding of MBL_3 oligomers to mcBSA-coupled surface with a simple 1:1 pseudo first-order reaction. The binding (S in RU) of oligomers in fraction I (*A*), fraction II (*B*), fraction III (*C*), fraction IV (*D*), and fraction V (*E*) to a surface with 1600 RU of mcBSA (*upper panels*) is indicated by black lines, together with the curves calculated according to Eq. 11 and 12 (gray lines). *Lower panels*, Difference (ΔS) between the experimental data (i.e., the sensorgrams) and the pseudo first-order reaction model. For all panels, this difference is also shown as the RMSD in a calculation involving the five or six sensorgrams and five or six calculated curves. The calculated K_D is indicated for each MBL_3 oligomer above each panel. *A*, Application of fraction I at c_{MBL3} concentrations (ascending order of sensorgrams) of 8, 16, 32, 64, and 96 nM. *B*, Application of fraction II oligomers at c_{MBL3} concentrations of 0.75, 1.5, 3, 6, 12, and 24 nM. *C*, Application of fraction III oligomers at c_{MBL3} concentrations of 0.5, 1, 2, 4, 8, and 16 nM. *D*, Application of fraction IV oligomers at c_{MBL3} concentrations of 0.625, 1.25, 2.5, 5, 10, and 20 nM. *E*, Application of fraction V oligomers at c_{MBL3} concentrations of 0.75, 1.5, 3, 6, 12, and 24 nM.

a global fitting of the sensorgrams (i.e., with single values of k_a, k_d, and S_{Max} accounting for the binding kinetics at all concentrations according to Eq. 11 and 12). The result of the modeling is shown with curves in gray ink (Fig. 4). For each of the applied concentrations, a curve was plotted according to Eq. 11 and 12 with the estimated values for k_a, k_d, and S_{Max}. For comparison, the corresponding experimental data (i.e., the sensorgrams) are indicated with solid black lines. In addition to visual inspection of the results, the goodness of the fit was evaluated by the root mean square deviation (RMSD) between the experimental and modeled data.

The sensorgrams in Fig. 4A and 4B, showing the binding of MBL oligomers in fractions I and II, differed significantly from curves plotted according to a 1:1 binding model. This observation was further indicated by large RMSD values. The sensorgrams for fractions III–V showed better agreement with the kinetics of a 1:1 binding model. However, a closer examination of the sensorgrams showed that the 1:1 binding model failed to account for a weak, but clearly discernible, curvature of the injection and dissociation phases (Fig. 4C–E). These phases were represented as essentially straight lines in the model. Consistent with the report by Teillet et al. (18), the 1:1 binding model failed to identify any major differences in terms of the calculated K_D. The apparent values for fractions II–V (Fig. 4B–E) were all at a level of $\sim 10^{-9}$ M. Only analysis of the oligomers in fraction I appeared to produce a significantly different result, with a K_D at 10^{-6} M. However, the accuracy of this estimation was questioned by the poor fit between the experimental data and the applied model.

Binding of MBL₃ oligomers analyzed by a model with continuous binding constant distributions

From the analysis made above, it was clear that the kinetics of the binding by the MBL₃ oligomers did not follow simple exponential functions, as defined by Eq. 11 and 12. As shown by the SAXS analysis (Table II), the ion-exchange chromatography fractions applied to the SPR experiments (i.e., fractions I–V) contained at least two types of MBL₃ oligomers (i.e., 3×MBL₃ and 6×MBL₃). We considered the possibility that binding of these MBL oligomers to the ligand-coupled surfaces comprised a heterogeneous ensemble of interactions originating from differences in the binding kinetics of the 3×MBL₃ and 6×MBL₃ oligomers. The data were analyzed by a recently developed model (30), which calculates the minimal distribution in kinetic parameters (i.e., k_a and k_d), required to account for the experimentally observed kinetics by assuming that the sensorgrams are a sum of multiple pseudo first-order reactions. The model has been applied in several other experimental analyses of heterogenous interactions (31, 32, 54, 55). For convenience in the interpretation of the distribution in binding strength, k_a was replaced by K_D, which is possible through the application of Eq. 10. The differential distribution of interactions P (k_d, K_D) can be formulated such that the integral P(k_d^*, K_D^*) $dk_d dK_D$ is the fractional abundance of interactions with a dissociation rate between k_d^* and $k_d^* + dk_d$ and a dissociation constant between K_D^* and $K_D^* + dK_D$. The time course of analyte binding in the association and dissociation phase is

$$S_{Tot}(c_{MBL_3}, t) = \int_{K_{D,min}}^{K_{D,max}} \int_{k_{d,min}}^{k_{d,max}} S(k_d, K_D, c_{MBL_3}, t)$$
$$P(k_d, K_D) dk_d dK_D, \quad (13)$$

where the function S is defined by Eq. 11 and 12 during the injection and dissociation phases, respectively (30).

In addition to the data already shown in Fig. 4, we included experiments to study the influence of ligand density on the binding

by the MBL₃ oligomers using surfaces coupled with 600 and 4000 RU of mcBSA (Fig. 5). The oligomers in fractions I (Fig. 5A–C), II (Fig. 5D–F), III (Fig. 5G–I), IV (Fig. 5J–L), and V (Fig. 5M–O) were injected in five or six concentrations over the three mcBSA-coupled surfaces and the reference surface, followed by subtraction of the signal generated by the reference flow cell from the signal in the mcBSA-coupled flow cells. The change in signal over the time course of the experiments is indicated by solid black lines. Application of the model with continuous binding constant distributions to these data demonstrated an excellent agreement between the experimental results and the curves calculated according to Eq. 13, with RMSD scores in the range of 0.25–11 RU (Fig. 5). The binding of the oligomers in fraction II to the surface with 4000 RU of mcBSA showed a larger RMSD value at 35 RU. However, compared with the maximum signal strength in this analysis of ~ 2400 RU, this still suggested a similar low relative difference between the model and the experimental data. In the case of the binding of the oligomers in fractions II and III, the RMSD scores were ~ 70- and 10-fold lower compared with the simple 1:1 binding model applied in Fig. 4.

The distribution of binding constants for the MBL₃ oligomers is shown in Fig. 6. Paired k_d and K_D values were plotted on the ordinate and abscissa, respectively, with a third dimension (indicated with contours) showing the abundance of interactions (in RU) with the indicated binding constants. The distribution of binding constants for the oligomers in fractions I (Fig. 6A–C), II (Fig. 6D–F), III (Fig. 6G–I), IV (Fig. 6J–L), and V (Fig. 6M–O) were shown for experiments using the three surfaces with 600, 1600, and 4000 RU of mcBSA. From this comparison, it was evident that an increase in oligomerization of MBL₃ or an increase in the ligand density increased the affinity by a lowering of k_d. In distinct contrast to the analysis with a simple 1:1 binding scheme (Fig. 4), the continuous binding constant model produced significant differences between the applied fractions. The oligomers bound mainly through two modes of interactions: one mode with K_D at $\sim 10^{-6}$ M and k_d at $\sim 10^{-2}$/s and another mode with K_D at $\sim 10^{-10}$–10^{-9} M and k_d at $\sim 10^{-5}$/s, as was particularly evident from a comparison of the binding of the oligomers in fraction V (Fig. 6J–L).

The influence of increasing oligomerization or ligand density primarily seemed to shift the binding from the low-affinity interaction to the high-affinity interaction. However, the influence of ligand density was only clear for the oligomers in fractions III–V (Fig. 6G–O). By contrast, the smaller oligomers in fractions I and II showed no striking sensitivity to ligand density with regard to the affinities of the interactions (Fig. 6A–F).

Several reports indicated that the binding of large proteins to ligands immobilized on gold-supported carboxymethylated dextran can be influenced by this matrix through mass transport effects. To directly investigate the contribution of the matrix to the observed binding kinetics, we made SPR chips with gold surfaces modified with a self-assembled layer of mercaptoundecanoic acid, which generates a layer of carboxylic acid groups for covalent coupling of mcBSA (or BSA in the reference cell). Binding of the MBL₃ oligomers in fractions I–V was easily observable in a flow cell coupled with 1600 RU of mcBSA (Fig. 7A, 7C, 7E, 7G, 7I) [i.e., at the same level used in flow cells modified with a dextran layer (Fig. 5B, 5E, 5H, 5K, 5N)]. The distribution in affinities was similar to the observations made earlier with ligands immobilized on dextran (Fig. 7B, 7D, 7F, 7H, 7J). The distribution in binding constants for the oligomers in fractions I and II peaked for interactions with K_D at $\sim 10^{-6}$–10^{-5} M and k_d at $\sim 10^{-2}$/s (Fig. 7B, 7D), similar to what was observed for these fractions applied to the dextran surfaces (Fig. 6B, 6E). For fractions III–V, this peak was also observed with the addition of a second peak with K_D
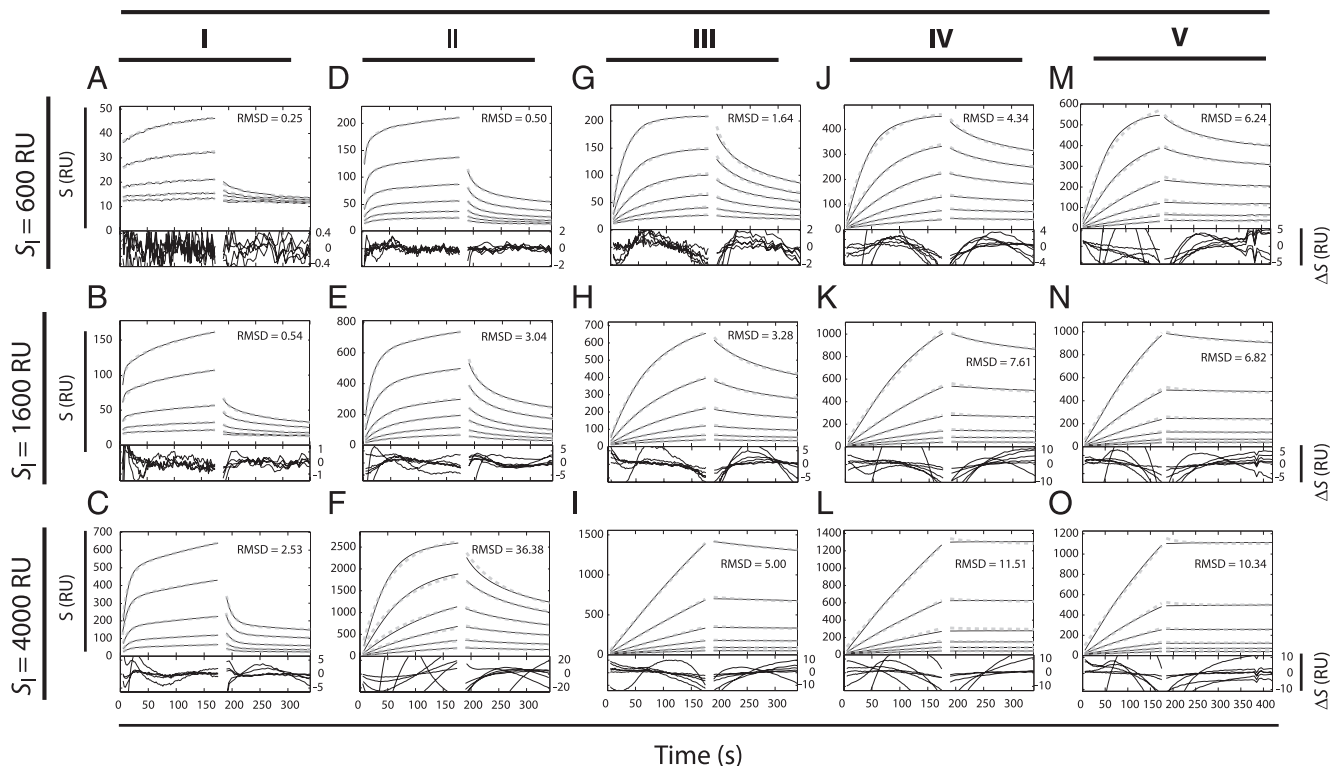
MBL ion exchange chromatography fraction

FIGURE 5. Analysis of the binding of MBL$_3$ oligomers to mcBSA-coupled surfaces analyzed by a model with a heterogeneous population of surface-binding sites with continuous binding-constant distributions. In addition to the sensorgrams shown in Fig. 3 for the binding of MBL$_3$ oligomers to a surface with 1600 RU of mcBSA, the binding sensorgrams for the interaction with surfaces presenting 600 and 4000 RU of mcBSA are shown. *Upper panels*, Sensorgrams are indicated by solid black lines, together with the curves calculated according to the model of heterogeneous populations of surface-binding sites (dashed gray lines). *Lower panels*, Difference (ΔS) between the sensorgrams and curves calculated according to the model. The RMSD is also indicated. Application of fraction I at c_{MBL3} concentrations (ascending order of sensorgrams) of 8, 16, 32, 64, and 96 nM to surfaces with 600 RU (*A*), 1600 RU (*B*), and 4000 RU (*C*) of mcBSA. Application of fraction II oligomers at c_{MBL3} concentrations of 0.75, 1.5, 3, 6, 12, and 24 nM to surfaces with 600 RU (*D*), 1600 RU (*E*), and 4000 RU (*F*) of mcBSA. Application of fraction III oligomers at c_{MBL3} concentrations of 0.5, 1, 2, 4, 8, and 16 nM to surfaces with 600 RU (*G*), 1600 RU (*H*), and 4000 RU (*I*) of mcBSA. Application of fraction IV oligomers at c_{MBL3} concentrations of 0.625, 1.25, 2.5, 5, 10, and 20 nM to surfaces with 600 RU (*J*), 1600 RU (*K*), and 4000 RU (*L*) of mcBSA. Application of fraction V oligomers at c_{MBL3} concentrations of 0.75, 1.5, 3, 6, 12, and 24 nM to surfaces with 600 RU (*M*), 1600 RU (*N*), and 4000 RU (*O*) of mcBSA.

at $\sim 10^{-10}$ M and k_d at $\sim 10^{-6}$–10^{-2}/s (Fig. 7*F*, 7*H*, 7*J*), with a slight sequestering of the second mode of interaction in the analysis of the binding with fraction V (Fig. 7*J*). As was the case for fractions I and III, the binding of oligomers in fractions III–V to ligands on the mercaptoundecanoic acid layer (Fig. 7*F*, 7*H*, 7*J*) closely matched the observations made with the dextran surfaces (Fig. 6*H*, 6*K*, 6*N*).

Structural and ligand-binding characteristics of recombinant (neck/CRD)$_3$

The ligand-binding characteristics of the (neck/CRD)$_3$ were studied similarly to the MBL$_3$ oligomers on surfaces with 600, 1600, and 4000 RU of mcBSA coupled to carboxymethylated dextran (Fig. 8). For all surfaces, the binding kinetics were fast, both during the injection phase and the dissociation phase (Fig. 8*A*, 8*C*, 8*E*). Compared with the MBL oligomers in fractions I–V, which were applied in the range of $c_{MBL3} \sim 10^{-9}$ M, the molar concentration required to generate a detectable binding of (neck/CRD)$_3$ was ~ 300-fold higher in the range of $c_{(neck/CRD)3} \sim 10^{-5}$ M. The sensorgrams were analyzed with the continuous binding constant distribution model as for the MBL$_3$ oligomers. Agreement between the experimental data and the model was excellent for all injections and surfaces (Fig. 8*A*, 8*C*, 8*E*), with RMSD at 0.27–2.07 RU. As judged from the contour plots, the distribution of interactions was relatively narrow. The model returned an estimate for K_D in the range

of 10^{-3}–10^{-2} M, with a $k_d \sim 10^{-2}$–10^{-1}/s for all surfaces (Fig. 8*B*, 8*D*, 8*F*).

Discussion

In this article, we reported that the higher-order oligomerization of MBL$_3$ and the ligand density of surfaces significantly influenced the binding properties of these complexes. Although this finding seems to be in agreement with a theoretical consideration over the properties of polyvalent binding, in contrast, experimental evidence previously suggested that 3×MBL$_3$ oligomers and larger complexes bind with essentially similar binding constants (18). Our observations have pertinence to the structural biology of MBL binding to target surfaces, as discussed below.

In the past, insight into the quaternary structure of MBL$_3$ oligomers was based on analyses with electron microscopy and AFM of surface-immobilized proteins. These investigations enabled high-resolution images of large MBL$_3$ oligomers (i.e., 4–8×MBL$_3$), but it was clearly a limiting factor that these oligomers were studied in the surface-adsorbed state. Dong et al. (15) derived the solution structure for 3×MBL$_3$ of rhMBL by application of SAXS. However, possibly as a consequence of the relative abundance of this oligomer in the sample, information was not extracted from the SAXS profiles on the larger oligomers. Based on the earlier-described procedures for size-fractionating MBL$_3$ oligomers using ion-exchange chromatography (8, 17, 18), we
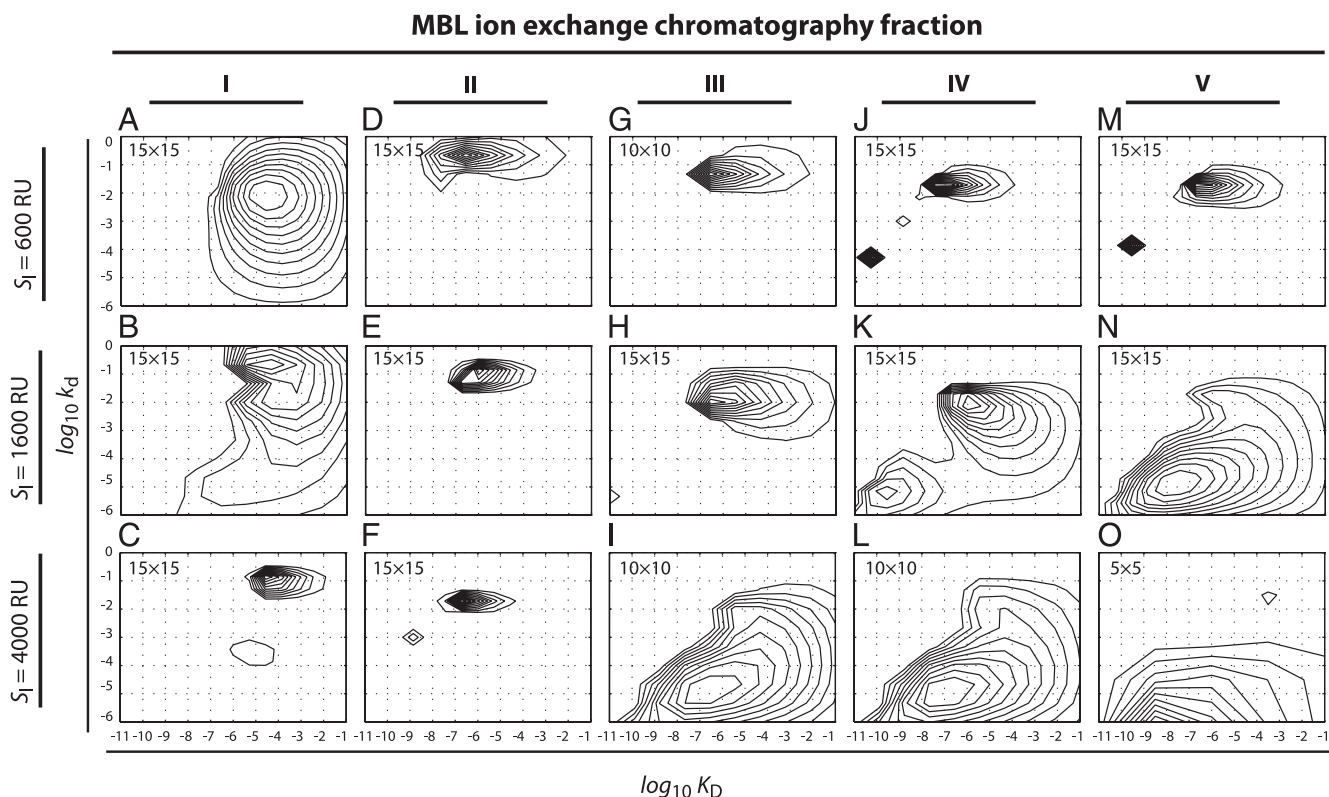
MBL ion exchange chromatography fraction

FIGURE 6. Continuous binding-constant distributions for the binding between MBL_3 oligomers and surfaces with three ligand densities. The binding-constant distribution is shown as a plot of the dissociation constant (K_D in M) and the dissociation, or "off", rate (k_d in s^{-1}), with the abundance at binding saturation (S in RU) of the classes of interaction indicated with contours. All calculations on the binding-constant distributions were made with K_D in the interval from 10^{-11} to 10^{-1} M and k_d in the interval from 10^{-6} to 1 s^{-1}. The number of grid points used to create the model is indicated in the upper left corner of each panel. Binding-constant distributions for the binding of MBL_3 oligomers in fraction I to surfaces with 600 RU (*A*), 1600 RU (*B*), and 4000 RU (*C*) of mcBSA. Binding-constant distributions for the binding of MBL_3 oligomers in fraction II to surfaces with 600 RU (*D*), 1600 RU (*E*), and 4000 RU (*F*) of mcBSA. Binding-constant distributions for the binding of MBL_3 oligomers in fraction III to surfaces with 600 RU (*G*), 1600 RU (*H*), and 4000 RU (*I*) of mcBSA. Binding-constant distributions for the binding of MBL_3 oligomers in fraction IV to surfaces with 600 RU (*J*), 1600 RU (*K*), and 4000 RU (*L*) of mcBSA. Binding-constant distributions for binding of MBL_3 oligomers in fraction V to surfaces with 600 RU (*M*), 1600 RU (*N*), and 4000 RU (*O*) of mcBSA.

modified this procedure to accommodate size-sorting of the MBL oligomers, as well as supplying fractions with a sufficient protein concentration to permit SAXS analyses. These analyses showed that there was an increment in the size of the eluting species with increasing salt concentration. Through the application of Eq. 2, SAXS measures the radius of gyration (R_G) very directly (47), which lends support to the robustness of the ultrastructural characterization of the molecules obtained in this way.

A more detailed view of the structure of the MBL_3 oligomers was made by pseudo-atomic modeling based on novel methods for the interpretation of SAXS data. Using MBL fractionation to enrich the larger oligomeric structures, it was possible, through SAXS analysis, to obtain information on the $6 \times MBL_3$, as well as the $3 \times MBL_3$, oligomers. By modeling a pool of conformers and selecting an ensemble matching the SAXS profile using the EOM, information on the distribution of R_G and D_{Max} was obtained, as well as a direct visualization of some of these conformers. With a modified EOM procedure, insight into the flexibility of the molecules was also permitted. In agreement with experimental evidence obtained from studies on collagen-like peptides (51), the collagenous parts of the MBL oligomers were modeled as rigid, whereas flexible linkers were connecting these in the C-terminal end to the $(neck/CRD)_3$ and in the N-terminal end to the hub bundling the MBL_3 structural units into oligomers. This procedure revealed a considerable variation in the relative orientation of the MBL_3 structural units. Also, the $(neck/CRD)_3$ fragment was ori-

ented in multiple ways relative to the rigid stalks, confirming earlier suggestions that this fragment is particularly flexible through an unfolded linker connecting the stalk and this fragment.

However, at least three points must be considered when interpreting these findings. First, in making the pool of conformers for selection by the EOM, these conformers were not subject to energy minimization or other procedures for avoiding strained conformations. In one attempt to carry out such an analysis on the conformational changes in IgM, which is of similar size to $6 \times MBL_3$, the energy changes associated with the conformational changes were small, unless obvious steric clashes were introduced (56). The conformers analyzed in our study did not present such clashes. Therefore, it seems reasonable to suggest that the selected conformations are acceptable approximations of species that would not violate energetic requirements. Second, a pool of $3 \times MBL_3$ and $6 \times MBL_3$ oligomers for selection by the EOM are obviously not permitting an exhaustive search for all types of oligomers found in the preparation. Nevertheless, it is clear that an ensemble of these two types of oligomers is sufficient to account for the SAXS data produced and a further inclusion of (e.g., $4 \times MBL_3$ and $5 \times MBL_3$) oligomers would consequently exhaust the information in the data, because the scattering properties of these oligomers are not sufficiently different from $3 \times MBL_3$ and $6 \times MBL_3$ to enable a distinction. Therefore, the pool of $3 \times MBL_3$ and $6 \times MBL_3$ oligomers represents small and large MBL_3 oligomers, which may be referred to as "$3 \times MBL_3$"-like and
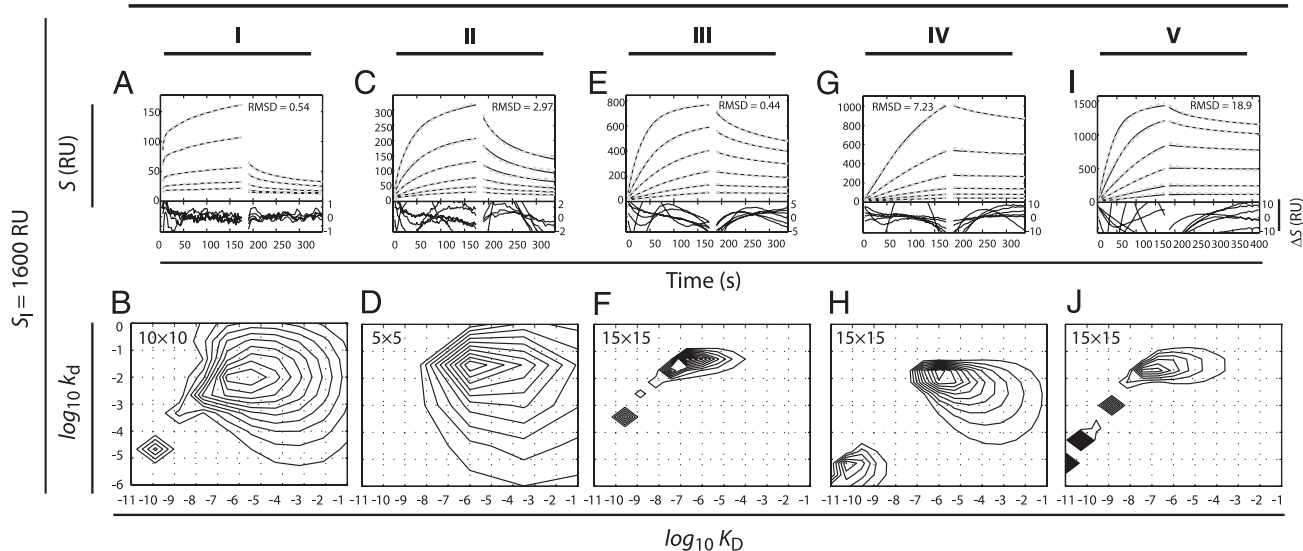
MBL ion exchange chromatography fraction

FIGURE 7. Analysis of the binding of MBL_3 oligomers to mcBSA-coupled gold surfaces modified with self-assembled layer of mercaptoundecanoic acid, analyzed by a model with a heterogeneous population of surface-binding sites with continuous binding-constant distributions. The surface was coupled with 1600 RU of mcBSA, followed by application of the rhMBL fractions I–V to these surfaces, as described for the application of surfaces with a dextran layer and coupled mcBSA. *A* and *B*, Application of fraction I at c_{MBL3} concentrations (ascending order of sensorgrams) of 8, 16, 32, 64, and 96 nM. *C* and *D*, Application of fraction II oligomers at c_{MBL3} concentrations of 0.75, 1.5, 3, 6, 12, and 24 nM. *E* and *F*, Application of fraction III oligomers at c_{MBL3} concentrations of 0.5, 1, 2, 4, 8, and 16 nM. *G* and *H*, Application of fraction IV oligomers at c_{MBL3} concentrations of 0.625, 1.25, 2.5, 5, 10, and 20 nM. *I* and *J*, Application of fraction V oligomers at c_{MBL3} concentrations of 0.75, 1.5, 3, 6, 12, and 24 nM.

"6×MBL_3"-like oligomers. The fractional abundance of these oligomers provides a crude estimate of the distribution in size, although not detailing the exact composition. Third, our analyses

suggested that a fraction of the 3×MBL_3 and 6×MBL_3 oligomers form larger assemblies that expand the oligomeric structure in a fashion different from the otherwise centrosymmetrical organi-

(neck/CRD)₃

FIGURE 8. The binding of (neck/CRD)₃ to mcBSA-coupled surfaces analyzed by a model with a heterogeneous population of surface binding sites shown together with the continuous binding-constant distributions for three surfaces with 600 RU (*A*, *B*), 1600 RU (*C*, *D*) and 4000 RU (*E*, *F*) of mcBSA. *A*, *C*, and *D*, Upper panels, Binding sensorgrams with the (neck/CRD)₃ applied at concentrations of (ascending order) 0.5, 1, 2, 4, 8, and 16 μM. Sensorgrams are shown in solid black lines, together with the calculated binding isotherms according to the heterogeneous population of surface binding sites model (dashed gray lines). Lower panels, Differences (Δ*S*) between the sensorgrams. This difference is also shown as the RMSD for a calculation involving the six sensorgrams and the binding isotherms of the model. *B*, *D*, and *F*, Continuous binding-constant distributions for the binding between MBL_3 oligomers and surfaces with three ligand densities. The binding-constant distribution is shown as a plot of K_D and k_d in s^{-1}, with the abundance of the classes of interaction indicated with contours. All calculations on the binding-constant distributions were made with K_D probed in the interval from 10^{-11} to 10^{-1} M and k_d probed in the interval from 10^{-6} to 1 s^{-1}. The number of grid points used to create the model is indicated in the upper left corner of each plot.
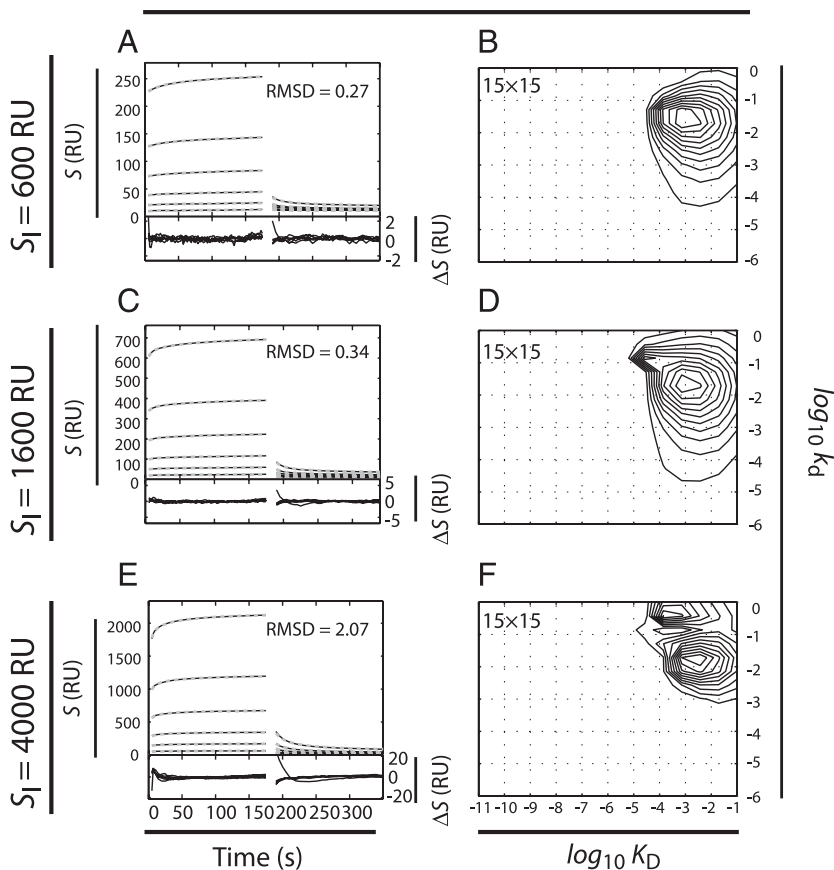
zation of the MBL$_3$ structural units. We found that a lateral association of these oligomers would create species with a SAXS profile that closely matched the experimental findings. Interestingly, the two interoligomeric distances in a trimeric assembly of 6×MBL$_3$ oligomers (i.e., 3 × 6×MBL$_3$) could be characterized with a single fitted value (d) that was quantitatively very similar to the single interoligomeric distance in a dimeric assembly (2 × 6×MBL$_3$), all at $d \sim 23$ nm. This type of assembly formation in MBL preparations has not been described earlier. We cannot exclude the possibility that such assemblies are influenced by the recombinant synthesis or fractionation of the MBL$_3$ oligomers. However, the uniformity of the interoligomeric distances found in these supramolecular assemblies suggests that the phenomenon is not a random process.

To translate our structural analysis into findings concerning the function of the MBL$_3$ oligomers, we investigated the binding kinetics by SPR spectroscopy. As demonstrated, the binding of MBL$_3$ oligomers to ligand-coupled surfaces is complex and not sufficiently described by a single 1:1 pseudo first-order reaction. This is entirely consistent with the expectations for a population of oligomers with heterogeneous binding constants and is indirect evidence that the oligomers indeed are different in their ligand binding. By applying a recent approach permitting an analysis of interactions with a continuous distribution of binding-kinetic constants (30), we showed that the binding by MBL$_3$ oligomers can be described as a composite of multiple 1:1 pseudo first-order reactions. An important requirement for this analysis is that the MBL$_3$ oligomers were applied to the surfaces in quantities not leading to saturation of binding sites, which would cause a significant influence from binding competition among the oligomers (30, 57). SPR sensorgrams for all surfaces clearly suggested that the surfaces were far from saturated with ligand, because all of the applied concentrations, including the highest one, caused large increments in the SPR signals. The oligomers bound mainly through two modes of interactions: one "low-affinity" mode, with a K_D at $\sim 10^{-6}$ M and k_d at $\sim 10^{-2}$/s and a "high-affinity" mode, with a K_D at $\sim 10^{-10}$–10^{-9} M and k_d at $\sim 10^{-5}$/s. The high-affinity mode was greatly supported by the application of ion-exchange chromatography fractions containing large oligomers, as shown by our analyses with SAXS. The low-affinity interactions were predominant when applying fractions containing a near-pure or a dominant population of 3×MBL$_3$. High-affinity binding was observed with the fractions presenting a near-pure population of 6×MBL$_3$. Compared with the low-affinity binding mode, the high-affinity mode differed by a 1000-fold decrease in k_d, whereas k_a was the same for both modes of interaction, as judged from Eq. 10. This observation is typical for strengthening of binding through avidity (57, 58). Consequently, the combined evidence suggested that the low- and high-affinity modes of binding reflected differences in avidity of the MBL$_3$ oligomers.

The contribution of CRD$_3$ to the calculated avidity of MBL$_3$ oligomers was analyzed by binding of the recombinant (neck/CRD)$_3$ fragment and suggested a K_D on the order of 10^{-3}–10^{-2} M with fast kinetics. This agrees well with the equilibrium constant at $K_D \sim 2.9 \times 10^{-3}$ M reported earlier for the binding of rat (neck/CRD)$_3$ to mannose monosaccharide, as studied by nuclear magnetic resonance (59, 60). In experiments using mannose as a competitor, Quesenberry et al. (61) described a half-maximum inhibitory concentration for these compounds at $\sim 2 \times 10^{-3}$ M; similar findings with mannose as a competitor was reported by Haurum et al. (62). It emerges from these earlier studies that the (neck/CRD)$_3$ constructs in our study bound the surface-coupled mcBSA with an affinity corresponding to the binding between a single CRD and a single mannose unit. Ng et al. (63) showed that

the CRD with the chelated Ca^{2+} ion binds mannose through coordination bonds in a sterically constrained fashion. Such constrains would not easily support binding by more than one CRD in the (neck/CRD)$_3$ to mannose residues on surface-immobilized mannosylated BSA. These findings readily suggested that the degree of MBL$_3$ oligomerization is the major source of avidity in the binding to the surfaces used in the current study.

Our analysis of the binding by the MBL$_3$ oligomers also offers insight on the role of ligand density. By using the transformation that 1000 RU equals 1 ng of surface-bound protein/mm^2 (64) and a formula weight for the mcBSA of 71,832 g/mol, the three surfaces with 600, 1600, and 4000 RU contained 0.005, 0.013, and 0.033 mcBSA molecules/nm^2, respectively. It was demonstrated earlier by AFM that the ligand-bound 3×MBL$_3$ oligomer in liquid spans a surface with a diameter of 60 nm (15). Using the numbers above and the surface area spanned by the MBL$_3$ oligomer (2826 nm^2), the average number of ligands in this area would be ~ 14, ~ 37, and ~ 93, with mean distances between the mcBSA molecules of ~ 14, ~ 9, and ~ 6 nm, respectively. This is on a scale that matches the size of the MBL$_3$ oligomers; our experimental investigations showed that the changes in ligand density on this level clearly affected the binding kinetics, with as much as a 300-fold difference in the observed dissociation rates. Although the larger "6×MBL$_3$"-like oligomers were able to bind with high affinity to a surface with ligands spaced 14 nm apart, this was not the case for the smaller oligomers. In contrast, the smaller oligomers could bind with high affinity to the surfaces with a denser presentation of ligands. These findings suggested that ligand presentation on the 10–20-nm scale may be an important structural feature in regulating MBL surface binding and could constitute a level of pattern recognition that has not been fully appreciated. The pattern recognition of this type is apparently regulated by the dimension of the MBL oligomers, suggesting the interesting possibility that the polydisperse nature of the MBL$_3$ oligomers, together with the surface exposure of ligands, has functional ramifications, although their biological significance remains to be studied. In this context, it is of considerable interest that recent studies of the bacterial cell wall of Gram-positive bacteria with AFM revealed repeating structural features (65, 66), or patterns, with a periodicity of 10–20 nm (65). In the case of Gram-negative *Pseudomonas aeruginosa*, the pili were similarly demonstrated by AFM to contain structural features at the nanometer scale (67). MBL appears to play a role in the defense against both of these microorganisms (68, 69). It is tempting to suggest that the nanometer-scaled ultrastructural organization of these microbial surfaces also reflects the surface presentation of the MBL ligands (i.e., a similar nanometer-scaled spacing of certain glycans). Consequently, the sensitivity of the MBL$_3$ oligomers to ligand spacing in the nanometer range is likely to play a role with regard to the binding of MBL to microbial surfaces and, hence, the function of MBL in the immune system. Similar to the surface binding by other large proteins of the humoral immune system, such as IgM (70, 71), for MBL there also appears to be a close link between the topological presentation of ligand and the outcome in terms of MBL deposition.

An important question not addressed in our experiments pertains to what influence the complex formation between the MBL$_3$ oligomers and the MASP would exert on the structural stability of the oligomer. SPR measurements found a tight binding of both MASP-1 and MASP-2 to MBL, with dissociation rates on the order of 5–6 × 10^{-4}/s (18). The binding site was mapped to the collagenous stalks (41, 72), which, in our study, were shown to exhibit a considerable variation in their relative orientation in the MASP-free state. With the propensity of the MASPs to form

homodimers (73) and recent x-ray crystallographic insight on collagen binding to MASP domains (74), it appears that MASP complexes with MBL involve bridging of MBL_3 structural units in the oligomer. Such a structural organization would clearly tie the relative orientation of these units. Other work (15) reported that the molecular geometry of the MBL_3 oligomers changed upon binding to ligands exposed on a surface compared with the structure found in solution. These findings point out that conformational changes in the MBL_3 oligomers, following binding to target surfaces, transmit a signal that potentially triggers MASP and, hence, complement activation. However, for such a mechanism to be meaningful, it would seem a logical prerequisite that the MBL/MASP complexes in solution assume a stable conformation. Although our studies showed that MASP-free MBL_3 oligomers are flexible, the evidence mentioned above indeed encourages the speculation that MASPs play a crucial role in supporting such conformational stability.

Acknowledgments

Disclosures

The authors have no financial conflicts of interest.

References

1. Fujita, T. 2002. Evolution of the lectin-complement pathway and its role in innate immunity. *Nat. Rev. Immunol.* 2: 346–353.
2. Holmskov, U., S. Thiel, and J. C. Jensenius. 2003. Collections and ficolins: humoral lectins of the innate immune defense. *Annu. Rev. Immunol.* 21: 547–578.
3. Vance, R. E., R. R. Isberg, and D. A. Portnoy. 2009. Patterns of pathogenesis: discrimination of pathogenic and nonpathogenic microbes by the innate immune system. *Cell Host Microbe* 6: 10–21.
4. Dommett, R. M., N. Klein, and M. W. Turner. 2006. Mannose-binding lectin in innate immunity: past, present and future. *Tissue Antigens* 68: 193–209.
5. Thiel, S., and M. Gadjeva. 2009. Humoral pattern recognition molecules: mannan-binding lectin and ficolins. *Adv. Exp. Med. Biol.* 653: 58–73.
6. Eisen, D. P. 2010. Mannose-binding lectin deficiency and respiratory tract infection. *J. Innate Immun.* 2: 114–122.
7. Ezekowitz, R. A., L. E. Day, and G. A. Herman. 1988. A human mannose-binding protein is an acute-phase reactant that shares sequence homology with other vertebrate lectins. *J. Exp. Med.* 167: 1034–1046.
8. Lu, J. H., S. Thiel, H. Wiedemann, R. Timpl, and K. B. Reid. 1990. Binding of the pentamer/hexamer forms of mannan-binding protein to zymosan activates the proenzyme C1r2C1s2 complex, of the classical pathway of complement, without involvement of C1q. *J. Immunol.* 144: 2287–2294.
9. Jensen, P. H., D. Weilguny, F. Matthiesen, K. A. McGuire, L. Shi, and P. Højrup. 2005. Characterization of the oligomer structure of recombinant human mannan-binding lectin. *J. Biol. Chem.* 280: 11043–11051.
10. Drickamer, K. 1992. Engineering galactose-binding activity into a C-type mannose-binding protein. *Nature* 360: 183–186.
11. Weis, W. I., K. Drickamer, and W. A. Hendrickson. 1992. Structure of a C-type mannose-binding protein complexed with an oligosaccharide. *Nature* 360: 127–134.
12. Weis, W. I., R. Kahn, R. Fourme, K. Drickamer, and W. A. Hendrickson. 1991. Structure of the calcium-dependent lectin domain from a rat mannose-binding protein determined by MAD phasing. *Science* 254: 1608–1615.
13. Sheriff, S., C. Y. Chang, and R. A. Ezekowitz. 1994. Human mannose-binding protein carbohydrate recognition domain trimerizes through a triple alpha-helical coiled-coil. *Nat. Struct. Biol.* 1: 789–794.
14. Weis, W. I., and K. Drickamer. 1994. Trimeric structure of a C-type mannose-binding protein. *Structure* 2: 1227–1240.
15. Dong, M., S. Xu, C. L. Oliveira, J. S. Pedersen, S. Thiel, F. Besenbacher, and T. Vorup-Jensen. 2007. Conformational changes in mannan-binding lectin bound to ligand surfaces. *J. Immunol.* 178: 3016–3022.
16. Jensenius, H., D. C. Klein, M. van Hecke, T. H. Oosterkamp, T. Schmidt, and J. C. Jensenius. 2009. Mannan-binding lectin: structure, oligomerization, and flexibility studied by atomic force microscopy. *J. Mol. Biol.* 391: 246–259.
17. Dahl, M. R., S. Thiel, M. Matsushita, T. Fujita, A. C. Willis, T. Christensen, T. Vorup-Jensen, and J. C. Jensenius. 2001. MASP-3 and its association with distinct complexes of the mannan-binding lectin complement activation pathway. *Immunity* 15: 127–135.
18. Teillet, F., B. Dublet, J. P. Andrieu, C. Gaboriaud, G. J. Arlaud, and N. M. Thielens. 2005. The two major oligomeric forms of human mannan-binding lectin: chemical characterization, carbohydrate-binding properties, and interaction with MBL-associated serine proteases. *J. Immunol.* 174: 2870–2877.
19. Mertens, H. D., and D. I. Svergun. 2010. Structural characterization of proteins and complexes using small-angle X-ray solution scattering. *J. Struct. Biol.* 172: 128–141.
20. Perkins, S. J., H. E. Gilbert, M. Aslam, J. Hannan, V. M. Holers, and T. H. Goodship. 2002. Solution structures of complement components by X-ray and neutron scattering and analytical ultracentrifugation. *Biochem. Soc. Trans.* 30: 996–1001.
21. Perkins, S. J., R. Nan, K. Li, S. Khan, and Y. Abe. 2011. Analytical ultracentrifugation combined with X-ray and neutron scattering: Experiment and modelling. *Methods* 54: 181–199.
22. Bernadó, P., E. Mylonas, M. V. Petoukhov, M. Blackledge, and D. I. Svergun. 2007. Structural characterization of flexible proteins using small-angle X-ray scattering. *J. Am. Chem. Soc.* 129: 5656–5664.
23. Piliarik, M., H. Vaisocherová, and J. Homola. 2009. Surface plasmon resonance biosensing. *Methods Mol. Biol.* 503: 65–88.
24. Montalto, M. C., C. D. Collard, J. A. Buras, W. R. Reenstra, R. McClaine, D. R. Gies, R. P. Rother, and G. L. Stahl. 2001. A keratin peptide inhibits mannose-binding lectin. *J. Immunol.* 166: 4148–4153.
25. McMullen, M. E., M. L. Hart, M. C. Walsh, J. Buras, K. Takahashi, and G. L. Stahl. 2006. Mannose-binding lectin binds IgM to activate the lectin complement pathway in vitro and in vivo. *Immunobiology* 211: 759–766.
26. Wallis, R. 2007. Interactions between mannose-binding lectin and MASPs during complement activation by the lectin pathway. *Immunobiology* 212: 289–299.
27. Karlsson, R., and A. Larsson. 2004. Affinity measurement using surface plasmon resonance. *Methods Mol. Biol.* 248: 389–415.
28. Schuck, P. 1997. Use of surface plasmon resonance to probe the equilibrium and dynamic aspects of interactions between biological macromolecules. *Annu. Rev. Biophys. Biomol. Struct.* 26: 541–566.
29. Sundberg, E. J., P. S. Andersen, I. I. Gorshkova, and P. Schuck. 2007. Surface plasmon resonance biosensing in the study of ternary systems of interacting proteins. In *Protein Interactions.* P. Schuck, ed. Springer US, New York, p. 97–141.
30. Svitel, J., A. Balbo, R. A. Mariuzza, N. R. Gonzales, and P. Schuck. 2003. Combined affinity and rate constant distributions of ligand populations from experimental surface binding kinetics and equilibria. *Biophys. J.* 84: 4062–4077.
31. Vorup-Jensen, T., C. V. Carman, M. Shimaoka, P. Schuck, J. Svitel, and T. A. Springer. 2005. Exposure of acidic residues as a danger signal for recognition of fibrinogen and other macromolecules by integrin alphaXbeta2. *Proc. Natl. Acad. Sci. USA* 102: 1614–1619.
32. Stapulionis, R., C. L. Oliveira, M. C. Gjelstrup, J. S. Pedersen, M. E. Hokland, S. V. Hoffmann, K. Poulsen, C. Jacobsen, and T. Vorup-Jensen. 2008. Structural insight into the function of myelin basic protein as a ligand for integrin alpha M beta 2. *J. Immunol.* 180: 3946–3956.
33. Chen, Z., P. Earl, J. Americo, I. Damon, S. K. Smith, F. Yu, A. Sebrell, S. Emerson, G. Cohen, R. J. Eisenberg, et al. 2007. Characterization of chimpanzee/human monoclonal antibodies to vaccinia virus A33 glycoprotein and its variola virus homolog in vitro and in a vaccinia virus mouse protection model. *J. Virol.* 81: 8989–8995.
34. Rosovitz, M. J., P. Schuck, M. Varughese, A. P. Chopra, V. Mehra, Y. Singh, L. M. McGinnis, and S. H. Leppla. 2003. Alanine-scanning mutations in domain 4 of anthrax toxin protective antigen reveal residues important for binding to the cellular receptor and to a neutralizing monoclonal antibody. *J. Biol. Chem.* 278: 30936–30944.
35. Vorup-Jensen, T. 2012. Surface plasmon resonance biosensing in studies of the binding between β_2 integrin I domains and their ligands. *Methods Mol. Biol.* 757: 55–71.
36. Vorup-Jensen, T., E. S. Sørensen, U. B. Jensen, W. Schwaeble, T. Kawasaki, Y. Ma, K. Uemura, N. Wakamiya, Y. Suzuki, T. G. Jensen, et al. 2001. Recombinant expression of human mannan-binding lectin. *Int. Immunopharmacol.* 1: 677–687.
37. Jensenius, J. C., P. H. Jensen, K. McGuire, J. L. Larsen, and S. Thiel. 2003. Recombinant mannan-binding lectin (MBL) for therapy. *Biochem. Soc. Trans.* 31: 763–767.
38. Jensen, L. E., S. Thiel, T. E. Petersen, and J. C. Jensenius. 1997. A rainbow trout lectin with multimeric structure. *Comp. Biochem. Physiol. B Biochem. Mol. Biol.* 116: 385–390.
39. Rossi, V., I. Bally, N. M. Thielens, A. F. Esser, and G. J. Arlaud. 1998. Baculovirus-mediated expression of truncated modular fragments from the catalytic region of human complement serine protease C1s. Evidence for the involvement of both complement control protein modules in the recognition of the C4 protein substrate. *J. Biol. Chem.* 273: 1232–1239.
40. Cseh, S., L. Vera, M. Matsushita, T. Fujita, G. J. Arlaud, and N. M. Thielens. 2002. Characterization of the interaction between L-ficolin/p35 and mannan-binding lectin-associated serine proteases-1 and -2. *J. Immunol.* 169: 5735–5743.
41. Teillet, F., M. Lacroix, S. Thiel, D. Weilguny, T. Agger, G. J. Arlaud, and N. M. Thielens. 2007. Identification of the site of human mannan-binding lectin involved in the interaction with its partner serine proteases: the essential role of Lys55. *J. Immunol.* 178: 5710–5716.

42. Pedersen, J. S. 2004. A flux- and background-optimized version of the Nano-STAR small-angle X-ray scattering camera for solution scattering. *J. Appl. Crystallogr.* 37: 369–380.

43. Schweinle, J. E., M. Nishiyasu, T. Q. Ding, K. Sastry, S. D. Gillies, and R. A. Ezekowitz. 1993. Truncated forms of mannose-binding protein multimerize and bind to mannose-rich *Salmonella montevideo* but fail to activate complement in vitro. *J. Biol. Chem.* 268: 364–370.

44. Shimaoka, M., C. Lu, R. T. Palframan, U. H. von Andrian, A. McCormack, J. Takagi, and T. A. Springer. 2001. Reversibly locking a protein fold in an active conformation with a disulfide bond: integrin alphaL I domains with high affinity and antagonist activity in vivo. *Proc. Natl. Acad. Sci. USA* 98: 6009–6014.

45. Fasman, G. D., ed. 1989. *CRC Practical Handbook of Biochemistry and Molecular Biology.* CRC Press, Boca Raton, FL.

46. Svergun, D. I., C. Barberato, and M. H. J. Koch. 1995. CRYSOL - a program to evalate X-ray solution scattering of biological macromolecules from atomic coordinates. *J. Appl. Crystallogr.* 28: 768–773.

47. Doniach, S. 2001. Changes in biomolecular conformation seen by small angle X-ray scattering. *Chem. Rev.* 101: 1763–1778.

48. Glatter, O. 1977. New method for evaluation of small-angle scattering data. *J. Appl. Crystallogr.* 10: 415–421.

49. Pedersen, J. S., S. Hansen, and R. Bauer. 1994. The aggregation behavior of zinc-free insulin studied by small-angle neutron scattering. *Eur. Biophys. J.* 22: 379–389.

50. Oliveira, C. L., M. A. Behrens, J. S. Pedersen, K. Erlacher, D. Otzen, and J. S. Pedersen. 2009. A SAXS study of glucagon fibrillation. *J. Mol. Biol.* 387: 147–161.

51. Fan, P., M. H. Li, B. Brodsky, and J. Baum. 1993. Backbone dynamics of (Pro-Hyp-Gly)10 and a designed collagen-like triple-helical peptide by 15N NMR relaxation and hydrogen-exchange measurements. *Biochemistry* 32: 13299–13309.

52. Orthaber, D., A. Bergmann, and O. Glatter. 2000. SAXS experiments on absolute scale with Kratky systems using water as a secondary standard. *J. Appl. Crystallogr.* 33: 218–225.

53. Karlsson, R., and A. Fält. 1997. Experimental design for kinetic analysis of protein-protein interactions with surface plasmon resonance biosensors. *J. Immunol. Methods* 200: 121–133.

54. Chen, Z., M. Moayeri, Y. H. Zhou, S. Leppla, S. Emerson, A. Sebrell, F. Yu, J. Svitel, P. Schuck, M. St Claire, and R. Purcell. 2006. Efficient neutralization of anthrax toxin by chimpanzee monoclonal antibodies against protective antigen. *J. Infect. Dis.* 193: 625–633.

55. Schmeisser, H., I. Gorshkova, P. H. Brown, P. Kontsek, P. Schuck, and K. C. Zoon. 2007. Two interferons alpha influence each other during their interaction with the extracellular domain of human type interferon receptor subunit 2. *Biochemistry* 46: 14638–14649.

56. Czajkowsky, D. M., and Z. Shao. 2009. The human IgM pentamer is a mushroom-shaped molecule with a flexural bias. *Proc. Natl. Acad. Sci. USA* 106: 14960–14965.

57. Kramer, R. H., and J. W. Karpen. 1998. Spanning binding sites on allosteric proteins with polymer-linked ligand dimers. *Nature* 395: 710–713.

58. Radnai, L., P. Rapali, Z. Hódi, D. Süveges, T. Molnár, B. Kiss, B. Bécsi, F. Erdödi, L. Buday, J. Kardos, et al. 2010. Affinity, avidity, and kinetics of target sequence binding to LC8 dynein light chain isoforms. *J. Biol. Chem.* 285: 38649–38657.

59. Iobst, S. T., and K. Drickamer. 1994. Binding of sugar ligands to Ca(2+)-dependent animal lectins. II. Generation of high-affinity galactose binding by site-directed mutagenesis. *J. Biol. Chem.* 269: 15512–15519.

60. Iobst, S. T., M. R. Wormald, W. I. Weis, R. A. Dwek, and K. Drickamer. 1994. Binding of sugar ligands to Ca(2+)-dependent animal lectins. I. Analysis of mannose binding by site-directed mutagenesis and NMR. *J. Biol. Chem.* 269: 15505–15511.

61. Quesenberry, M. S., R. T. Lee, and Y. C. Lee. 1997. Difference in the binding mode of two mannose-binding proteins: demonstration of a selective minicluster effect. *Biochemistry* 36: 2724–2732.

62. Haurum, J. S., S. Thiel, H. P. Haagsman, S. B. Laursen, B. Larsen, and J. C. Jensenius. 1993. Studies on the carbohydrate-binding characteristics of human pulmonary surfactant-associated protein A and comparison with two other collectins: mannan-binding protein and conglutinin. *Biochem. J.* 293: 873–878.

63. Ng, K. K., A. R. Kolatkar, S. Park-Snyder, H. Feinberg, D. A. Clark, K. Drickamer, and W. I. Weis. 2002. Orientation of bound ligands in mannose-binding proteins. Implications for multivalent ligand recognition. *J. Biol. Chem.* 277: 16088–16095.

64. Stenberg, E., B. Persson, H. Roos, and C. Urbaniczky. 1991. Quantitative-determination of surface concentration of protein with surface-plasmon resonance using radiolabelled proteins. *J. Colloid Interface Sci.* 143: 513–526.

65. Touhami, A., M. H. Jericho, and T. J. Beveridge. 2004. Atomic force microscopy of cell growth and division in *Staphylococcus aureus. J. Bacteriol.* 186: 3286–3295.

66. Verbelen, C., N. Christiaens, D. Alsteens, V. Dupres, A. R. Baulard, and Y. F. Dufrêne. 2009. Molecular mapping of lipoarabinomannans on mycobacteria. *Langmuir* 25: 4324–4327.

67. Touhami, A., M. H. Jericho, J. M. Boyd, and T. J. Beveridge. 2006. Nanoscale characterization and determination of adhesion forces of *Pseudomonas aeruginosa* pili by using atomic force microscopy. *J. Bacteriol.* 188: 370–377.

68. Møller-Kristensen, M., W. K. Ip, L. Shi, L. D. Gowda, M. R. Hamblin, S. Thiel, J. C. Jensenius, R. A. Ezekowitz, and K. Takahashi. 2006. Deficiency of mannose-binding lectin greatly increases susceptibility to postburn infection with *Pseudomonas aeruginosa. J. Immunol.* 176: 1769–1775.

69. Takahashi, K., L. Shi, L. D. Gowda, and R. A. Ezekowitz. 2005. Relative roles of complement factor 3 and mannose-binding lectin in host defense against infection. *Infect. Immun.* 73: 8188–8193.

70. Vorup-Jensen, T., and T. Boesen. 2011. Protein ultrastructure and the nanoscience of complement activation. *Adv. Drug Deliv. Rev.* 63: 1008–1019.

71. Pedersen, M. B., X. Zhou, E. K. Larsen, U. S. Sørensen, J. Kjems, J. V. Nygaard, J. R. Nyengaard, R. L. Meyer, T. Boesen, and T. Vorup-Jensen. 2010. Curvature of synthetic and natural surfaces is an important target feature in classical pathway complement activation. *J. Immunol.* 184: 1931–1945.

72. Wallis, R., A. W. Dodds, D. A. Mitchell, R. B. Sim, K. B. Reid, and W. J. Schwaeble. 2007. Molecular interactions between MASP-2, C4, and C2 and their activation fragments leading to complement activation via the lectin pathway. *J. Biol. Chem.* 282: 7844–7851.

73. Feinberg, H., J. C. Uitdehaag, J. M. Davies, R. Wallis, K. Drickamer, and W. I. Weis. 2003. Crystal structure of the CUB1-EGF-CUB2 region of mannose-binding protein associated serine protease-2. *EMBO J.* 22: 2348–2359.

74. Gingras, A. R., U. V. Girija, A. H. Keeble, R. Panchal, D. A. Mitchell, P. C. Moody, and R. Wallis. 2011. Structural Basis of Mannan-Binding Lectin Recognition by Its Associated Serine Protease MASP-1: Implications for Complement Activation. *Structure* 19: 1635–1643.